Published in final edited form as:
Biochemistry. 2019 April 16; 58(15): 1992–2008. doi:10.1021/acs.biochem.9b00050.

Crystallographic Structures of IlvN·Val/Ile Complexes: Conformational Selectivity for Feedback Inhibition of Aceto Hydroxy Acid Synthases

Akanksha Bansal[†], **N. Megha Karanth**[†,‖], **Borries Demeler**[‡], **Hermann Schindelin**[*,§], **Siddhartha P. Sarma**[*,†,#]

[†] Molecular Biophysics Unit, Indian Institute of Science, Bangalore, Karnataka 560012, India

[‡] Department of Biochemistry and Structural Biology, The University of Texas Health Science Center at San Antonio, Mailcode 7760, 7703 Floyd Curl Drive, San Antonio, Texas 78229-3900, United States

[§] Rudolf Virchow Centre for Experimental Biomedicine, Institute of Structural Biology, University of Wuerzburg, Josef-Schneider-Strasse 2, D-97080 Wuerzburg, Germany

[#]NMR Research Center, Indian Institute of Science, Bangalore, Karnataka 560012, India

Abstract

Conformational factors that predicate selectivity for valine or isoleucine binding to IlvN leading to the regulation of aceto hydroxy acid synthase I (AHAS I) of *Escherichia* coli have been determined for the first time from high-resolution (1.9–2.43 Å) crystal structures of IlvN·Val and IlvN·Ile complexes. The valine and isoleucine ligand binding pockets are located at the dimer interface. In the IlvN·Ile complex, among residues in the binding pocket, the side chain of Cys^{43} is 2-fold disordered (χ_1 angles of *gauche*$^-$ and *trans*). Only one conformation can be observed for the identical residue in the IlvN·Val complexes. In a reversal, the side chain of His^{53}, located at the surface of the protein, exhibits two conformations in the IlvN·Val complex. The may play an important role in the regulation of the AHAS I holoenzyme activity. A significant result is the establishment of the subunit composition in the AHAS I holoenzyme by analytical ultracentrifugation. Solution nuclear magnetic resonance and analytical ultracentrifugation experiments have also provided important insights into the hydrodynamic properties of IlvN in the ligand-free and -bound states. The structural and biophysical data unequivocally establish the molecular basis for differential binding of the ligands to IlvN and a rationale for the resistance of IlvM to feedback inhibition by the branched-chain amino acids.

---

[*] **Corresponding Authors:** hermann.schindelin@virchow.uni-wuerzburg.de. Phone: +49 931 31-80382. Fax: +49 931 31-87320. sidd@iisc.ac.in. Phone: +91 80 2293 3454. Fax: +91 80 23600535.
[‖] **Present Address:** N.M.K.: Institut für Organische Chemie, Leibniz Universität, Hanover, Germany.

Supporting Information
The Supporting Information is available free of charge on the ACS Publications website at DOI: 10.1021/acs.biochem.9b00050.

The authors declare no competing financial interest.

Accession Codes
The structural and coordinates of IlvN·Val and IlvN·Ile complexes have been deposited in the RCSB Protein Data Bank as entries 5YPP [IlvN·Val (1a)], 5YPW [IlvN·Val (1b)], 5YPY [IlvN·Val (1c)], and 5YUM [IlvN·Ile (2)]. The Uniprot ID for IlvN is P0ADF8.

Graphical Abstract

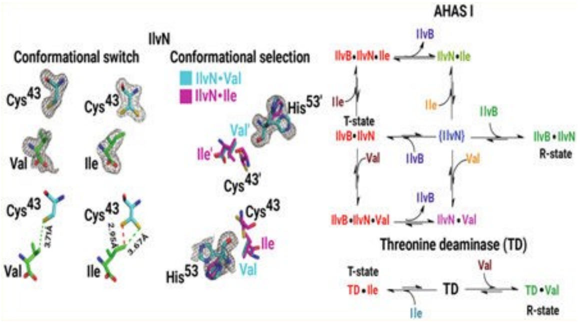

The biosynthesis of the branched-chain amino acids, isoleucine, leucine, and valine, begins with enzyme-catalyzed "acyloin-like" condensation reactions of either two molecules of pyruvate or one molecule each of pyruvate and 2- ketobutyrate to form 2-acetolactate or 2-aceto-2-hydroxybuty- rate, respectively,[1,2] by the multisubunit enzyme aceto hydroxy acid synthase (AHAS, EC 2.2.1.6).[3] The former product is then channeled into the biosynthesis of valine and leucine, while the latter is channeled into the biosynthesis of isoleucine. The formation of 2-acetolactate and 2-aceto-2-hydroxybutyrate constitutes the first and committed step in the biosynthesis of branched-chain amino acids. Enterobacteria such as *Escherichia coli* and *Salmonella typhimurium* have three isozymes known as AHAS I, II, and III[4,5] that are encoded by the genes ilvBN,[6,7] ilvGM,[8] and ilvIH,[9–11] respectively, where genes B, G, and I encode the catalytic subunits (CSUs) and N, M, and H encode the regulatory subunits (RSUs). Other bacteria possess an equivalent of AHAS III as the sole enzyme catalyzing this committed step. The structure of the catalytic subunit[12–15] and the catalytic and kinetic properties of the enzyme have been studied over several decades.[16,17] AHAS I is essential for valine and isoleucine biosynthesis when *E. coli* is grown under conditions of nutrient stress, viz., when acetate or succinate is the sole source of carbon.[18] AHAS II and AHAS III are optimally active under conditions of high intracellular concentrations of pyruvate.[18] Furthermore, they have a strong preference for 2-ketobutyrate over pyruvate as the second substrate[19,20] with specificity ratios of 60 and 40, respectively.[21] In contrast, AHAS I has a low specificity for 2-ketobutyrate[22,23] (specificity ratio of 1–3).

The RSUs play a dual role in that they are responsible for activation of CSU and regulation of enzyme activity. The latter occurs through binding of the effector molecules (end products of the pathway) to allosteric binding sites on the RSUs. In prokaryotes, the effector is usually valine and to a far lesser extent leucine and isoleucine.[3,22] In enterobacteria, AHAS I is strongly feedback inhibited by valine while AHAS III is 60–80% inhibited at saturating concentrations of valine. AHAS II is valine resistant.

In contrast to the sequence and structural conservation seen for the catalytic subunits, the regulatory subunits are diverse. The three-dimensional X-ray structures of *E. coli* IlvH[24] and its orthologs from *Thermotoga maritima* and *Nitrosomonas europea*[25] have shown the N-terminal domains of these proteins to fold as ACT domains.[3,26–29] Furthermore, these ACT domains of AHAS I and III exhibit highly ordered structures in the absence of "effector molecules". The binding sites of the effector molecules have been inferred from sequence and structural homology of the regulatory subunits to the ACT domain of D-3-phosphoglycerate dehydrogenase.[30] The structure of the ACT subunit of AHAS I was determined by our group recently[31] using solution nuclear magnetic resonance (NMR) spectroscopic methods [Protein Data Bank (PDB) entry 2LVW]. We had shown that, in the free form, IlvN exists in an ensemble of states whose conformations have been difficult to define. In the presence of valine, IlvN experiences significant conformational reordering, exists as a dimer with the ACT fold, and is similar to the ligand-free state of the ACT domain of IlvH.[24] The regulatory subunit has significantly different affinities for the three amino acids. The structural data available thus far provide few atomistic details about the structural basis for this selectivity, given the small differences in chemistry of the effector molecules. Importantly, the mechanism by which activation and regulation of the holoenzyme are brought about by structural and conformational changes in the RSUs is yet to be deciphered.[32]

As part of our ongoing investigations of the structure of the AHAS I holoenzyme, we have obtained high-resolution crystal structure data of complexes of IlvN with valine and isoleucine. We have also probed the solution conformation properties of the CSU, RSU, and the holoenzyme using analytical ultra-centrifugation. The crystal structures unequivocally establish the molecular basis for differential binding to valine and isoleucine by IlvN. The stoichiometry of association of the CSU and RSU in the holoenzyme has been established by analytical ultracentrifugation. By comparison of the high-resolution structures determined here, the rationale for the resistance of IlvM to feedback inhibition by the branched-chain amino acids is proposed. Data from analytical ultracentrifugation experiments also provide a qualitative estimate of the affinity of IlvN for the effector molecules and insight into the physical forms of the protein in the ligand-free and -bound states.

■ EXPERIMENTAL PROCEDURES

Protein Expression and Purification.

Purification of IlvN was carried out using the protocol described previously.[33,34] Chemicals used for protein purification were purchased from Sigma-Aldrich, Merck, and other local suppliers. The columns and matrices for size exclusion, ion-exchange, and IMAC chromatography were purchased from GE Healthcare and Bio-Rad. Protein concentrations were estimated from absorbance measurements at 280 nm carried out on a double-beam Varian Cary 100 ultraviolet–visible (UV–vis) spectrophotometer.

Crystallographic Studies.

Crystallization kits, paraffin oil, and silicon oil from Hampton Research were used for crystallizing the protein under different conditions using the microbatch method. Microbatch plates were purchased from local vendors. IlvN and IlvB proteins for crystallization trials were dialyzed against 20 mM potassium phosphate buffer (pH 7.4), 20 mM NaCl, 1 mM EDTA, and 0.01% sodium azide. Diffraction quality crystals of IlvN·Val and IlvN·Ile complexes were obtained under the conditions listed in Table S1.

Diffraction data for IlvN crystals in the presence of valine were collected with a MARmosaic 225 CCD detector at a wavelength of 0.9537 Å and 100 K on beamline BM14 at the European Synchrotron Radiation Facility (ESRF, Grenoble, France), while data for IlvN crystals in the presence of isoleucine were obtained at 100 K using an in-house Rigaku R-axis IV++ diffractometer equipped with a FR-E$^+$ SuperBright UltraHigh Intensity MicroFocus Rotating Anode X-ray generator and a Rigaku R-AXIS IV++ low-noise imaging plate detector.

Structure Solution and Refinement.—The structure of IlvN in crystal form 1a was determined by molecular replacement using the program *Phaser*[35] as implemented in the *CCP4i*[36] software suite. A Matthews coefficient of 2.31 Å^3/Da, corresponding to a solvent content of 46.7%, led to a search for six molecules of IlvN in the asymmetric unit.[37] The solution NMR structure of IlvN (PDB entry 2LVW) was used as the starting model to solve the phase problem. Refinement with *REFMAC*[38] or 25 cycles resulted in R_{work} and R_{free} values of 0.4543 and 0.4757, respectively. Electron densities were missing for eight residues at the N-terminus, and this region was removed from the template structure. Residues at the C-terminus showed poor model fitting and hence were also removed, and the structure was further refined. With this, the R_{work} and R_{free} decreased by 5% to 0.3809 and 0.4217, respectively. In the next step, a search for the orientation of the C-terminal helix[31] using the program *ARP/wARP*[39] was executed. Electron density corresponding to the C-terminal helix was traced perpendicular to the four-stranded β-sheet. The resulting model was refined for 100 cycles resulting in R_{work} and R_{free} values of 0.2771 and 0.307, respectively. The improvement in refinement factors confirmed the validity of model rebuilding. As the asymmetric unit was found to have six molecules, refinement was carried out with NCS restraints that decreased the R factors by 1% to values of 0.2662 and 0.2970, respectively. The ligand and solvent were fit by incorporating TLS restraints.[40] Refinement of resulting structures with the ligand and solvent gave values of 0.2333 and 0.2643 for R_{work} and R_{free}, respectively. As the initial L-test carried out using the program AIMLESS suggested twinning, further refinement was carried out using intensity-based twinning refinement that decreased R_{work} and R_{free} values by 8% giving values of 0.1559 and 0.1819, respectively. The final refinement and model building were carried out using the *phenix·refine* module,[41] which resulted in a structure with R_{work} and R_{free} values of 0.1484 and 0.1703, respectively. A similar protocol was followed to determine the ligand-bound structures of IlvN in crystal forms **1b**, **1c**, and **2**.

Structure Analysis.—The three-dimensional structures of the IlvN·Val and IlvN·Ile complexes were analyzed using *Coot, PyMOL*,[42] *UCSF Chimera*,[43] and *MOLMOL*.[44] Packing densities were calculated using *Voronoia*.[45] Internal cavities and their volumes were calculated using *CastP*.[46]

Hydrodynamic Studies by Analytical Ultracentrifugation (AUC).

Instrumentation.—The AUC sedimentation velocity studies of IlvN in the absence and presence of ligands, valine and isoleucine, were carried out using a Beckman Coulter ProteomeLab XL-A analytical ultracentrifuge equipped with an analytical An-60 Ti four-place rotor and absorbance optics. Analytical sample cells with standard double-sector charcoal-filled Epon centerpieces with a thickness of 12 mm and a length of 14 mm fitted with quartz windows were used. Samples were centrifuged at 42000 rpm. Protein sedimentation was monitored at 20 °C at either 230 or 280 nm using intensity detection. The buffer density and viscosity were determined from the buffer composition as calculated by *UltraScanIII*, version 4.0 (revision 2492 for Windows),[47,48] and partial specific volumes were calculated from the partial amino acid composition with tools available in *UltraScanIII*.

Sample Preparation.—Samples of IlvN for AUC studies were prepared in phosphate buffer (1.8 mM monobasic potassium phosphate, 10 mM dibasic sodium phosphate, 137 mM sodium chloride, and 2.7 mM potassium chloride). Sedimentation velocity experiments with IlvN in the free and ligand-bound states were carried out at IlvN concentrations ranging from 4.2 to 180 μM. Protein sedimentation was monitored at 230 and 280 nm at low (<25 μM) and high (>25 μM) concentrations of IlvN, respectively. The absorbance measurements were carried out using a double-beam Varian Cary 100 UV−vis spectrophotometer using water as a blank. The absorbance for analytes in the reference channel was maintained below 0.5 while that for the sample channel solution was ≤1. Details of the protein and ligand concentrations for each SV-AUC run are listed in Table S2. Sedimentation velocity experiments with IlvB were carried out at an IlvB concentration of 20 μM. The holoenzyme samples were prepared using 8 μM IlvB and 58 μM IlvN. Samples were prepared in phosphate buffer (1.8 mM monobasic potassium phosphate, 10 mM dibasic sodium phosphate, 137 mM sodium chloride, and 2.7 mM potassium chloride) with additional 10 mM $MgCl_2$ in IlvB buffer. The absorbance values for IlvB and holoenzyme samples were 0.73 and 0.65, respectively, at 280 nm. The samples were centrifuged prior to the AUC studies at 13000 rpm to remove any particulate matter. They were later filtered through a 0.22 μm syringe filter prior to being loaded into the analytical cells.

Sedimentation Velocity Data Analysis.—SV-AUC analysis was carried out using *UltraScanIII*. The experimental data were processed as described by Demeler[49] using two-dimensional spectrum analysis (2DSA)[50] and further refined by parsimonious regularization using genetic algorithm (GA) analysis.[51,52] Integral sedimentation distributions were calculated using the enhanced van Holde and Weischet method.[53]

Homology Modeling Studies of IlvM.

Homology modeling was carried out for an input target sequence of *E. coli* IlvM, the regulatory subunit of the AHAS II isozyme, using the web-based SWISS-MODEL program.[54] The crystal structure of IlvH, the regulatory subunit of the AHAS III isozyme (PDB entry 2F1F), was chosen as the template, based on the target–template alignment score, for generation of a homology model. The quality of the built model was assessed using the QMEAN[55] scoring function.

■ RESULTS AND DISCUSSION

Analysis of SV-AUC Data.

IlvN in the Free State.—In the free form, IlvN is heterogeneous in its oligomerization state. A dimer–tetramer equilibrium can be observed in the GA analysis plots of the SV-

AUC data (Figure 1, i and ii). The tetramer (molecular weight of 45 kDa) sediments at 3.2 S and has a frictional coefficient of 1.4, while the dimer sediments at 2.4 S with a frictional coefficient of 1.2. At low IlvN concentrations (<8 μM), the two species are present in nearly equal proportions. The dimer:tetramer ratio decreases with an increase in protein concentration. At high IlvN concentrations (≥170 μM), the equilibrium shifts towards the higher-molecular weight tetrameric species (Figure 1, ii).

IlvN in the Presence of Valine and Isoleucine.—IlvN in the presence of valine sediments as a dimer with a molecular weight of 25 kDa, a sedimentation coefficient of 2.5 S, and an f/f_o of 1.21 (Figure 1, iii). The change in sedimentation coefficient on going from the free to the bound form indicates a transition from dimer/tetramer to dimer species with concomitant structural changes seen in earlier solution studies.[31] IlvN shows a low affinity for isoleucine compared to that for valine, and this was apparent from SV experiments. At isoleucine concentrations 30- and 70-fold higher than that of IlvN, the protein behaves as though in the unbound state. A high proportion of species with molecular weights of 45 and 32.3 kDa (weight-average molecular weight due to a dimer– tetramer equilibrium), sedimenting at 3.1 and 2.8 S, respectively, were observed. A lower proportion of species with molecular weights of 27 and 22.4 kDa (dimeric state), sedimenting at 2.6 and 2.2 S, respectively, are indicative of a weaker affinity of IlvN for isoleucine. When isoleucine was present at concentrations >100-fold greater than that of IlvN, a single species with a molecular weight of 25 kDa sedimenting at 2.5 S and an f/f_o of 1.2 was observed (Figure 1, iv). Significantly higher (10-fold) concentrations of isoleucine are required for IlvN to mirror the hydrodynamic behavior of the IlvN·Val complex (Figure S1).

IlvB and AHAS I Holoenzyme.—IlvB, in the presence of cofactors, ThDP, FAD, and Mg^{2+} sediments as a dimer with a molecular weight of 120 kDa with a sedimentation coefficient of 6.2 S and a frictional coefficient of 1.3 (Figure 1, v). This form has been observed at concentrations of ≤20 μM. IlvB is known to be catalytically competent,[32] and it is safe to conclude that this catalytically competent form is dimeric in nature.

The AHAS I holoenzyme sediments at 7.8 S and has a molecular weight of ~160 kDa, indicating that the IlvB and IlvN subunits are present in a 2:4 ratio (Figure 1, vi).

Crystallographic Studies.

Crystallization trials with IlvN in the presence of valine resulted in crystal growth under several different conditions. The crystals were platelike in all of the cases and took 3–4 weeks to grow. Of these, three crystals diffracted well and varied in the number of molecules present in the asymmetric unit and the space group in two cases (Figure S2). The IlvN·Ile complex also crystallized under different conditions, but good diffraction quality data could be obtained for only one, which allowed structure solution. The data collection, refinement, and structural statistics for the four crystal structures determined in this study are listed in Table 1, and a portion of a model fit into the electron density map is displayed in Figure 2.

The structures of IlvN in the four crystal forms are dimeric in nature and are nearly identical to each other. Pairwise superposition of the backbone atoms of chain A of 1a on the corresponding atoms of chains A of 1b, 1c, and 2 showed root-mean-square deviations

(RMSDs) of 0.48, 0.47, and 0.52 Å, respectively. The average temperature factors for all atoms for all four models (1a–1c and 2) after the final refinement were found to be 42, 47, 52, and 53 Å^2, respectively. The interiors of the proteins are well-packed and show packing densities of 0.71, 0.70, 0.70, and 0.70, respectively.

Protomer Structure.

Each protomer is formed by three α helices, $\alpha1$ (residues 23–32), $\alpha2$ (residues 63–73), and $\alpha3$ (residues 89–97), and four β strands, $\beta1$ (residues 10–18), $\beta2$ (residues 40–45), $\beta3$ (residues 52–59), and $\beta4$ (residues 77– 82), arranged in a $\beta1$–$\alpha1$–$\beta2$–$\beta3$–$\alpha2$–$\beta4$–$\alpha3$ ferredoxin like fold (Figure S3A). This topology is typical of ACT proteins[27] and is identical to that observed in the solution NMR structure of IlvN (PDB entry 2LVW)[31] and the N-terminal domain of IlvH (*vide infra*). Helix $\alpha3$ at the C-terminus is perpendicular to the long axis (y-axis) of the β sheet and extends out like a hook from the rest of the molecule. The perpendicular arrangement is favored by strong hydrophobic interactions between Met^{89}, Phe^{90}, and Ile^{93} of $\alpha3$ and Leu^{42} of $\beta2$ and Trp^{55} and Leu^{57} of $\beta3$ (Figure S3B), and a tight packing is observed among $\alpha1$, $\alpha2$, and the central β sheet (Figure S3C). The antiparallel arrangement of the β sheet is maintained by an extensive network of hydrogen bonding interactions (discussed below).

Dimer Structure and Comparison with IlvH.

Our crystallographic studies indicate that IlvN exists as a dimer in all of the crystal forms studied here. The structure of IlvN is similar in the presence of valine and isoleucine. The dimer is constructed from two chains that are related by a 2-fold axis of symmetry (Figure 3, i). The dimer interface is formed by helices $\alpha1$, $\alpha3$, and strand $\beta2$ from chain A and helices $\alpha1'$, $\alpha3'$, and strand $\beta2'$ from chain B (Figure 3, ii). The ACT subunit comprising two protomers of IlvN has a core formed by an eight-stranded antiparallel β sheet (Figure 3, iii). The β sheet is sandwiched by four helices ($\alpha1$, $\alpha2$, $\alpha1'$, and $\alpha2'$) on one face and by helices $\alpha3$ and $\alpha3'$ on the other. Dimerization results in 2676 Å^2 of buried surface area.

IlvN is structurally similar to the N-terminal domain of IlvH (the regulatory subunit of AHAS III).[24] The two polypeptides show a sequence identity of 30%, each with an identical topology, except at the C-terminus. The backbone super- position of IlvN (C^{α} atoms) on the N-terminal ACT domain of IlvH (PDB entry 2f1f) resulted in RMSD values of 1.08, 1.22, 1.19, and 1.16 Å for crystal structures 1a–1c and 2, respectively. Large deviations in RMSD are seen in the C- terminal region of the two proteins. The C-terminal helix of IlvN ($\alpha3$) coincides with strand $\beta5$, i.e., the first secondary structural element of the C-terminal domain of IlvH (residues 80–163). IlvN too has no known stable monomeric form and like the homologous IlvH is a likely candidate for three- dimensional domain swapping[57] (Figure S4).

Hydrogen bonding interactions between strands $\beta2$ and $\beta2'$ (Figure 3, iii) and hydrophobic interactions among helices $\alpha1$, $\alpha1'$, $\alpha3$, and $\alpha3'$ (Figure 3, ii) contribute significantly to the stability of the dimer. Met^{89}, Ile^{93}, and Phe^{97} of helix $\alpha3$ are involved in hydrophobic interactions with symmetry-related Phe^{97}, Ile^{93}, and Met^{89} of helix $\alpha3'$. The hydrophobic patch enclosed by helices $\alpha3$ and $\alpha3'$ and strands $\beta2$, $\beta2'$, $\beta3$, and $\beta3'$ further maintain dimer integrity. Leu^{42} and Leu^{44} from $\beta 2$ and Trp^{55} and Leu^{57} from $\beta 3$ interact with Ala^{94} of $\alpha 3$ and with Met^{89}, Phe^{90}, Ile^{93}, and Phe^{97} of $\alpha 3'$ (Figure S5). Significant differences in the structures of IlvN·Val, IlvH (PDB entry 2f1f), and IlvN determined by solution NMR (PDB entry 2lvw) are observed for this region of the protein.

PEG Molecules at the Dimer Interface.

IlvN crystal 1a was obtained in the presence of 30% PEG 4000 (Table S1). Three PEG fragments were modeled for each dimer in the asymmetric unit (Figure S6A). Of these, one is located at the dimer interface (PEG 101) between helices $\alpha 3$ of the two protomers. This PEG molecule is stabilized by hydrophobic interactions with phenylalanine residues from both chains (Figure S6B, i). PEG molecules 102 and 103 are related by 2- fold symmetry and are present at the intramonomer interface formed by helix $\alpha 3$ and strand $\beta 2$. They are stabilized mainly via hydrophobic interactions with aliphatic and polar amino acid residues (Figure S6B, ii and iii) from chains A and B, respectively. PEG molecule 102 is also seen to interact via hydrogen bonding with the main chain of Phe^{90}. Crystal form 1b, which was also crystallized in the presence of PEG, does not show electron density for this co-solute. The presence or absence of PEG does not appear to influence the structure of IlvN.

Cobalt Binding Pocket.

The crystal structure of the IlvN· Ile complex (2) shows each dimer coordinated to one cobalt ion (Figure 4, i) which resides on the crystallographic 2-fold symmetry axis. An anomalous difference map revealed a very strong density at the position of the cobalt ion (Figure S7), and this was observed even at a level of 26 times the RMSD. The imidazole N$^{\delta}$1 atom of His^{20} and the O$^{\delta}$1 atom of Asp^{76} and its counterparts in the other subunits coordinate Co^{2+} in what appears to be significantly distorted tetrahedral geometry (Figure 4, ii). The complex is further stabilized through additional electrostatic interactions with the O$^{\delta}$2 atoms of Asp^{76} that are positioned 3.42 Å from the Co^{2+} ion. Duggleby and co-workers[17] had reported that the ACT subunits of *E. coli* AHAS II exhibit an intrinsic affinity for metal binding, and this property was used to facilitate purification of native IlvM from cell extracts. The structures determined here provide a rationale for their observation.

Comparison with Solution NMR Studies of IlvN.

The most notable difference between the solution NMR structure of IlvN[31] and the X-ray structures determined here is in the orientation of C-terminal helices $\alpha 3$ and $\alpha 3'$ (Figure 5, i and ii). In the X-ray structure, this helix is arranged perpendicular to the β sheet axis (Figure 5, i). In the NMR structure, the helix lies parallel to the β sheet axis (Figure 5, ii).

Back-calculation of the expected NOE correlations based on the X-ray structure of the IlvN·Val complex indicates that a set of NOE correlations that involve Phe^{97} and Gln^{98} (C-terminal residues) with residues His^{53} and Trp^{55} (Figure 5, iii) should be present in the NMR NOESY data. However, we have not observed these NOEs in ^{15}N- and ^{13}C-edited three-dimensional NOESY data. Thus, the NMR structure is not compatible with a domain-swapped C-terminal helix. Domain swapping has not been observed in other ACT domains such as in NikR (PDB entry 1q5y),[58] tyrosine hydroxylase (PDB entry 3mda),[59] or 3-phosphoglycerate dehydrogenase (PDB entry 1psd).[60]

Additional NMR data that rely on long-range order such as RDCs, paramagnetic shifts, and PRE may be necessary to unequivocally establish whether the C-terminal helix is domain swapped. As we will show below, the orientation of the C- terminal helix has little bearing on the mechanism of binding and feedback regulation.

Ligand Binding Pockets in the Crystal Structures.

Feedback regulation of AHAS I in *E. coli* occurs through binding of the end products of the metabolic pathway to the regulatory subunit IlvN. Figure 6 shows the changes in line widths, as observed in the one-dimensional NMR spectrum of IlvN in the presence of valine, isoleucine, leucine, and threonine. Significant changes in the line shape can be observed upon binding of valine and isoleucine. However, very little change can be observed upon addition of leucine (≤100 mM) or threonine (≤20 mM), indicating that IlvN does not bind either of these amino acids. Crystallization studies have produced structural data for the IlvN·Val and IlvN·Ile complexes. IlvN has two ligand binding pockets located at the dimer interface[61] that are related by the 2-fold symmetry axis of the dimer.

The geometries of the binding pockets are nearly identical for both valine and isoleucine as observed in all four crystal forms of IlvN, further validating the ligand binding positions. Figure 7 shows the omit maps defining the electron densities (panels i and iii) of the ligand molecules in their respective binding pockets and the anatomies of the ligand binding pockets in the four crystal forms.[62,62] The ligands are held tightly by means of hydrogen bonding and hydrophobic interactions.

For both valine (panels ii, v, and vi) and isoleucine (panel iv), the carboxyl group is involved in five hydrogen bonding interactions, three with the backbone nitrogens of Val^{23} and Met^{24} (both chain B) and Val^{38} (chain A). The other two occur as water-mediated hydrogen bonds with the backbone atoms of Gly^{22} and Thr^{25} (both chain B) and Phe^{36} (chain A). The amine group is hydrogen bonded to the side chains of Asn^{19} (chain B) and Asn^{37} (chain A) and the backbone of Val^{38} (chain A).

The side-chain groups of valine are anchored by hydro-phobic interactions with the aliphatic side chains of residues from chain B, viz., Val^{17}, His^{20}, Pro^{21}, and Cys^{43}. Similarly, the side-chain groups of isoleucine show hydrophobic interactions with the aliphatic side chains of residues from chain B, viz., His^{20}, Pro^{21}, Cys^{43}, Ser^{52}, and Ile^{41} (chain A). Valine in crystal form 1c shows additional hydrophobic interactions with Ile^{41} (chain A).

The valine/isoleucine binding pocket described here corroborates the model of the binding pocket constructed by Kaplun et al.[24] for IlvH, using the serine-bound structure of 3PGDH[30] as a template, which is also corroborated by mutational studies.[24,32,63] The model of the IlvH binding pocket correctly predicts the participation of residues Asn^{29} and Ile^{30} from across the dimeric interface in stabilizing the bound ligand. In the case of IlvN, it is Asn^{37} and Val^{38} that perform a similar role. It also predicts the hydrophobic interaction between Leu^{9}, which is equivalent to Val^{17} in IlvN, and the ligand. However, the model did not predict the role of Gly^{22} and Thr^{25} from chain B and Phe^{36} from chain A in stabilizing the bound ligand via water-mediated hydrogen bonds. Furthermore, neither the hydrogen bond between Val^{23} (Ala^{15} in IlvH) and the ligands nor the role of His^{20} and Pro^{21} (Glu^{12} and Ser^{13} in IlvH) in stabilizing the ligands in the binding pocket was foreseen.

In all, the model predicted valine to be stabilized by four hydrogen bonds, while the experimental observations here suggest a total of 14 (13 in the case of the IlvN·Ile complex) hydrogen bonds, depending on the crystal form. The presence of two conserved water molecules in the ligand binding pocket in all four structures underscores their structural importance. Indeed, mutation of the highly conserved Gly^{14} in IlvH (Gly^{22} in IlvN) results in ACT subunits that are insensitive to valine. Other mutations in IlvH that either retain or cause loss of valine sensitivity can also be rationalized from the structural features of the ligand-bound form of IlvN.

Valine versus Isoleucine versus Leucine.

Enzymatic studies have shown that the sensitivity of AHAS I to feedback inhibition by the end products of the metabolic pathway decreases in the order valine > isoleucine > leucine with apparent K_i values of 11 ± 3 μM for valine and 223 μM for isoleucine in the case of IlvH.[24] The K_d for the IlvN·Val complex is ~23 μM.[31] Our attempts to determine the K_d for the IlvN·Ile complex have not met with success due to the propensity of the protein to aggregate at the very high concentration of the protein required for ITC experiments. The structural data described above are indicative of a commonality of structural features that are sufficient for binding of either valine or isoleucine by IlvN and are indicative of a tightly packed binding pocket.

The spatial orientation of the ε-methyl group of Met^{24} exhibits a significant variation in the four structures, with χ_3 values of 86.8° (1a), −172.7° (1b), 166.3° (1c), and −84.22° (2) (Figure 8) indicative of the plasticity of the binding pocket. Distances from the $C^{Val}\gamma 2/^{Ile}\gamma 1$ atoms of the ligands to the ε-methyl group range from 4.4 Å in 1a to 5.8 Å in 1c and 6.5 Å in 1b and 2. An interesting and consistent observation is the orientation of the γ-sulfhydryl group of Cys^{43} in the four crystal forms. In the valine-bound structures, the χ_1 angle for this residue is *gauche*$^-$ (−61.4°) and this changes to trans (179.5°) when isoleucine is present in the binding pocket. This reorientation is necessary to avoid a steric clash between the γ-sulfhydryl group and the δ-methyl group of isoleucine. Of significance is the fact that isoleucine has only a 50% occupancy, and consequently, both orientations of the γ-sulfhydryl can be observed in the structure (Figure 8). In mutational studies carried out with IlvH, it was observed that residues Leu^{9}, Leu^{16}, and Val^{35} are responsible for the differential affinities of IlvH for the three effector molecules. Mutations of Leu^{16} and Val^{35} to amino acids with less bulky side chains increased the sensitivity for the ligand isoleucine.[24]

In IlvN, the corresponding residues are Val^{17}, Met^{24}, and Cys^{43}. While Val^{17} and Met^{24} are part of the binding pocket, the conformation of Cys^{43} is important for conferring selectivity for valine or isoleucine. Furthermore, it can be inferred that in the case of the amino acid leucine, either of the two χ_1 conformations observed for Cys^{43} will result in the steric exclusion of the isopropyl methyl groups of leucine. Interestingly, the B-factors for residues in the binding pocket for the IlvN·Ile complex are higher than those of the corresponding residues in the IlvN·Val complex. This is consistent with the observations described above. The *B*- factors for the backbone C^{α} atoms for structures 1a and 2 are listed in Table S3.

There is a complete correspondence in the residues involved in the ligand pocket of both the X-ray structure determined here and solution NMR titration studies.[31] Panels i and ii of Figure 9 show the chemical shift perturbation upon titration of the IlvN·Ile complex with valine. A total of 23 residues showed a chemical shift perturbation of >0.05 ppm (Figure 9, iii). Of these, residues in $\alpha 1$, $\beta 2$, and $\beta 3$ show significant perturbation. It was also observed that the resonance lines of the N-terminal residues of helix $\alpha 1$, viz., Met^{24}, Thr^{25}, and His^{26}, are missing in the ^{1}H–^{15}N HSQC spectrum presumably due to line broadening effects of chemical exchange. The X-ray crystallo-graphic studies have enabled a precise understanding of the orientation of the ligand in the binding pocket and important structural features such as water-mediated hydrogen bonds that are essential for the binding and/or stability of the effector molecules in the binding pocket.

Homology Modeling Studies of IlvM.

The model for the IlvM dimer compared with the structure of the IlvN·Val complex (1a) is shown in panel i of Figure 10. For reference, the sequence alignment used in the model generation is also shown (Figure 10, ii)). Residues in IlvM that coincide with those of the ligand binding pocket in IlvN are Ala^{10}, Phe^{12}, Asp^{13}, Pro^{14}, Glu^{15}, Thr^{16}, Leu^{17}, Glu^{18}, and Met^{36} of chain B of IlvM and Phe^{29}, His^{30}, and Val^{31} of chain A. The significant changes in IlvM, due to sequence dissimilarity (Figure 10, iii) of the two polypeptides, are Phe^{12} in place of Asn^{19}, His^{30} in place of Asn^{37}, and Met^{36} in place of Cys^{43}.

The implications of these changes are (i) an increase in steric bulk in the ligand binding pocket and (ii) a loss of hydrogen bond acceptor groups. The volumes of the binding pockets in IlvN and the modeled structure of IlvM are 300 and 134 Å^3, respectively. In contrast, the volumes of valine, leucine, and isoleucine are 140, 165, and 165 Å^3, respectively; hence, the volume of the binding pocket in IlvM is comparable to the volume of both amino acids. This significant reduction could explain the loss of valine/isoleucine/leucine sensitivity. Interestingly, during the course of our studies, we had serendipitously cloned an Asn^{37} → Tyr mutant[64] of IlvN from *E. coli* genomic DNA. Unlike wild-type IlvN, this particular mutant was able to activate IlvB but was insensitive to valine.[64] The loss of valine sensitivity caused by this mutation is consistent with the analysis described above.

The regulatory subunits of the enterobacterial AHASs provide a platform for examining the effects of amino acid substitutions that result in differential and/or different affinity for the effector molecules and ultimately the effect of these natural sequence variations on the mechanism of allosteric regulation. On the basis of our understanding of the structures of the ACT subunits of IlvN and the ACT domain of IlvH and the presence of the amino acid substitutions in IlvM mentioned above, it is unclear if IlvM behaves as an ACT regulatory subunit. However, it has also been shown convincingly that IlvM can cross-activate IlvB and IlvH.[32] Several attempts to render the IlvM protein amenable to structural studies by solution NMR methods in our laboratory have been unsuccessful. Future studies of the structure and function of IlvM will shed light on this aspect of the regulatory subunit of AHAS II.

■ DISCUSSION

The enterobacterial AHAS isozymes present several unique structural and enzymatic properties. It is well established that the catalytic subunits of these enzymes are similar in sequence and structure and catalyze identical reactions in all species of bacteria, fungi, and plants. In contrast, the regulatory subunits are diverse in sequence and structure. In particular, the regulatory subunits of AHAS I and II are small, single-domain polypeptides that dimerize to form ACT subunits.

In the studies described above, we have shown through high- resolution crystal structures that the ACT subunit of AHAS I binds the branched-chain amino acids valine and isoleucine. The detection of one or the other of these amino acids in four crystal structures obtained under varying solute and co-solute conditions unequivocally establishes the locus of binding. Further proof is obtained from the fact that the physicochemical characteristics of binding are once again nearly identical. Solution NMR, analytical ultracentrifugation, and kinetics of inhibition of enzyme activity in conjunction with mutagenesis established that the affinity of the ACT subunit for the branched-chain amino acids decreases in the following order: valine > isoleucine > leucine.[24]

Comparisons of structures of IlvN in the Val- and Ile-bound forms show that the conformation of the Cys^{43} side chain is the deciding factor that determines the specificity for Val or Ile. Though this change is imperative to accommodate isoleucine, other changes accompanying effector binding are also observed. Just as the Cys^{43} (β2) side chain is observed in two conformations in the Ile-bound structure, the His^{53} (β3) imidazole ring also shows two conformations in the valine- bound structure. There appears to be a concerted conformational change in the side chains of Cys^{43} and His^{53} (Figure 11, i).

Studies of the competitive binding of valine and isoleucine to IlvN in solution have shown that both Cys^{43} and His^{53} exhibit significant chemical shift perturbation when valine displaces isoleucine from the binding pocket (cf. panel i of Figure 9). It must be kept in mind that the protein exists in an ensemble of conformational states in the free form and that ligands are in fast exchange on the NMR time scale in the bound form. Other residues spatially proximal to His^{53} also show significant chemical shift perturbations (cf. panel ii of Figure 9). Several of these residues have backbone amide atoms that are 9–10 Å from the cysteine side chain, and they appear to be clustered on one edge of a cube (Figure S8). The question that arises here is whether this conformational change has any bearing on the activation or regulation of holoenzyme activity. The ligand binding pocket itself is capacious and could easily accommodate either valine or isoleucine without significant perturbation. Thus, it is meaningful to assume that conformational selection in the solution state may determine effector selectivity.

Using solution NMR studies, our group had shown that IlvN interacts with the α and β domains of IlvB.[64] These studies have been supported by recent biophysical and mutagenesis studies of the RSU−CSU interactions of *E. coli* AHASs.[65] Thus, the CSU−RSU interaction is proposed to occur at the α–β interface on IlvB, with the residues on IlvN described above being the region of contact.

An allosteric model for the regulation of AHAS I isozyme activity has been proposed by Chipman and co-workers.[16,66] In this model, inhibition does not occur via dissociation of the catalytic and regulatory subunits upon valine or isoleucine binding. They propose that the holoenzyme may exist in an inactive “T” state that may be either IlvB·IlvN·Val or IlvB·IlvN (low activity), and an active “R” state (IlvB·IlvN) exists, which has a low sensitivity for the inhibitory effects of valine or isoleucine at the allosteric site. Keeping in mind this nondissociative mechanism, we attempted to crystallize the holoenzyme in the presence of the effector molecules. A similar mechanism has been proposed for threonine deaminase activity, wherein the enzyme has a high and low affinity for valine and isolecuine, respectively, in the active “R” state and vice versa for the inactive “T” state. It is interesting to note that although AHAS I has a low specificity for 2-ketobutyrate, the enzyme binds isoleucine and causes inhibition of the biosynthesis of valine and leucine. The structural data from this study should enable a better understanding of the binding of these effector molecules to the ACT domains of threonine deaminase (for which no structural data exist) and their role in regulation of this enzyme.

An alternate mechanism for the regulation of AHAS I would involve dissociation of the holoenzyme into catalytic and regulatory subunits upon binding of valine or isoleucine. Here conformational changes in IlvN upon binding of valine or isoleucine would lower the stability of the holoenzyme. The competing mechanisms are summarized in a schematic representation in panel ii of Figure 11.

The structures of ACT domains of several enzymes and transcription factors have been determined in the absence or presence of effector molecules.[28,29] Despite a low level of sequence homology among the proteins that form ACT domains, there is remarkable structural homology in topology and fold. As we have inferred in case of IlvM, selectivity towards effector molecules must then be conferred by modulation of volume of the binding pocket, to accommodate effector molecules of varying steric bulk.[61] A remarkable example is the simultaneous binding of lysine and threonine to ACT domains formed by asymmetric association of non-equivalent ACT domains formed from different subunits (AK II *Corynebacterium glutamicum*) and the same subunits (AK III, *Synechocystis*), respectively.[28,67–69]

In conclusion, the high-resolution structures of the IlvN·Val and IlvN·Ile complexes determined here have enabled the unequivocal identification of the binding sites of the effector molecules. Analyses of the structures indicate that the observed differences in side-chain conformations of residues in the binding pocket and its vicinity confer selectivity for activation or inhibition of holoenzyme activity and that conformational exchange in solution may determine effector selectivity. The structural role of these amino acids at other check points in the pathway, viz., catalysis of threonine deamination by threonine deaminase and formation of 2-isopropylmalate by 2-isopro-pylmalate synthase, must be taken into consideration to gain a better understanding of the biosynthesis and regulation of branched-chain amino acid production. Insights into the mechanism of activation or inhibition, via dissociative or nondissociative processes of the AHAS (I) holoenzyme, can be formulated only from future high-resolution biophysical and structural studies of the holoenzyme.

Supplementary Material

Refer to Web version on PubMed Central for supplementary material.

ACKNOWLEDGMENTS

The X-ray facilities at the Molecular Biophysics Unit supported by the Science and Engineering Research Board, Department of Science and Technology (DST), India, and access to beamline BM-14 at ESRF supported by funds from the Department of Biotechnology (DBT), India, are gratefully acknowledged. A.B. and S.P.S. thank DBT and DST India for the Mass Spectrometry and NMR facilities at the Indian Institute of Science. A.B. and S.P.S. also thank the Chairperson, Department of Biochemistry, Indian Institute of Science. for use of the analytical ultracentrifuge. The development of UltraScan was supported by National Institutes of Health Grant GM120600 and National Science Foundation (NSF) Grant ACI-1339649 (both to B.D.). Supercomputer calculations were performed on Comet at the San Diego Supercomputing Center (supported by NSF/XSEDE Grant TG-MCB070039N to B.D.) and Lonestar-5 at the Texas Advanced Computing Center (supported by UT Grant TG457201 to B.D.).

Funding

A.B. is supported by a University Grants Commission Senior Research Fellowship. A.B. is grateful to the DAAD student visitor fellowship program. This work is supported by a DST Grant (EMR/2015/001178) to S.P.S.

ABBREVIATIONS

■

NMR	nuclear magnetic resonace
NOE	nuclear Overhauser effect
PDB	Protein Data Bank
SV-AUC	sedimentation velocity-analytical ultracentrifugation
GA	genetic algorithm
ACT	domain, aspartokinase, chorismate mutase, and TyrA

■ REFERENCES

(1). Umbarger HE, and Brown B (1958) Isoleucine and Valine Metabolism in Escherichia coli: VIII. The Formation of Acetolactate. J. Biol. Chem 233, 1156–1160. [PubMed: 13598751]

(2). Willson CD, and Adelberg EA (1957) The Biosynthesis Of Isoleucine and Valine: IV. Accumulation of Citramalic and α,β - Dimethylamalic Acids by a Neurospora mutant. J. Biol. Chem 229, 1011–1018. [PubMed: 13502360]

(3). McCourt JA, and Duggleby RG (2006) Aceto Hydroxy Acid Synthase and its role in the biosynthetic pathway for branched-chain amino acids. Amino Acids 31, 173–210. [PubMed: 16699828]

(4). Guardiola J, De Felice M, Lamberti A, and Iaccarino M (1977) The Acetolactate Synthase isoenzymes of Escherichia coli K-12. Mol. Gen. Genet 156, 17–25. [PubMed: 340888]

(5). Guardiola J, Felice MD, and Iaccarino M (1974) Mutant of Escherichia coli K-12 Missing Acetolactate Synthase Activity. J. Bacteriol 120, 536–538. [PubMed: 4608700]

(6). Wek RC, Hauser CA, and Hatfield GW (1985) The nucleotide sequence of the ilvBN operon of Escherichia coli: Sequence homologies of the Aceto Hydroxy Acid Synthase isozymes. Nucleic Acids Res 13, 3995–4010. [PubMed: 2989782]

(7). Newman T, Friden P, Sutton A, and Freundlich M (1982) Cloning and expression of the ilvB gene of Escherichia coli K-12. Mol. Gen. Genet 186, 378–384. [PubMed: 6181375]

(8). Lawther RP, Wek RC, Lopes JM, Pereira R, Taillon BE, and Hatfield GW (1988) The complete nucleotide sequence of tbe ilvGMEDA operon of Escherichia coli K-12. Nucleic Acids Res 16, 3602.

(9). Felice MD, Guardiola J, Esposito B, and Iaccarino M (1974) Structural Genes for a Newly Recognized Acetolactate Synthase in Escherichia coli K-12. J. Bacteriol 120, 1068–1077. [PubMed: 4612003]

(10). Squires CH, De Felice M, Lago CT, and Calvo JM (1983) ilvIH locus of Salmonella typhimurium. J. Bacteriol 154, 1054–1063. [PubMed: 6189818]

(11). Squires CH, DeFelice M, Devereux J, and Calvo JM (1983) Molecular structure of ilvIH and its evolutionary relationship to ilvG in Escherichia coli K12. Nucleic Acids Res 11, 5299–5313. [PubMed: 6308579]

(12). Pang SS, Duggleby RG, and Guddat LW (2002) Crystal structure of yeast Aceto Hydroxy Acid Synthase: a target for herbicidal inhibitors. J. Mol. Biol 317, 249–262. [PubMed: 11902841]

(13). McCourt JA, Pang SS, King-Scott J, Guddat LW, and Duggleby RG (2006) Herbicide-binding sites revealed in the structure of plant acetohydroxyacid synthase. Proc. Natl. Acad. Sci. U. S. A 103, 569–573. [PubMed: 16407096]

(14). Lonhienne T, Garcia MD, Pierens G, Mobli M, Nouwens A, and Guddat LW (2018) Structural insights into the mechanism of inhibition of AHAS by herbicides. Proc. Natl. Acad. Sci. U. S. A 115, E1945–E1954. [PubMed: 29440497]

(15). Garcia MD, Nouwens A, Lonhienne TG, and Guddat LW (2017) Comprehensive understanding of Aceto Hydroxy Acid Synthase inhibition by different herbicide families. Proc. Natl. Acad. Sci. U. S. A 114, E1091–E1100. [PubMed: 28137884]

(16). Barak Z, and Chipman DM (2012) Allosteric regulation in Aceto Hydroxy Acid Synthases (AHASs)–different structures and kinetic behaviour in isozymes in the same organisms. Arch. Biochem. Biophys 519, 167–174. [PubMed: 22198286]

(17). Hill MC, Pang SS, and Duggleby GR (1997) Purification of Escherichia coli Aceto Hydroxy Acid Synthase isoenzyme II and reconstitution of active enzyme from its individual pure subunits. Biochem. J 327, 891–898. [PubMed: 9581571]

(18). Umbarger HE1996 Biosynthesis of the branched-chain amino acids in Escherichia coli and Salmonella In Escherichia coli and Salmonella: Cellular and Molecular Biology (Neidhardt R, Curtiss JL III, Ingraham ECC, Lin KB, Low B, Magasanik WS, Reznikoff M, Riley M, Schaechter HE, and Umbarger HE; Eds.) 2 ed., pp 442–457, ASM Press: Washington DC.

(19). Gollop N, Damri B, Barak Z, and Chipman DM (1989) Kinetics and mechanism of acetohydroxy acid synthase isozyme III from Escherichia coli. Biochemistry 28, 6310–6317. [PubMed: 2675968]

(20). Gollop N, Damri B, Chipman D, and Barak Z (1990) Physiological implications of the substrate specificities of acetohydroxy acid synthases from varied organisms. J. Bacteriol 172, 3444–3449. [PubMed: 2345154]

(21). Epelbaum S, LaRossa RA, VanDyk TK, Elkayam T, Chipman DM, and Barak Z (1998) Branched-chain amino acid biosynthesis in Salmonella typhimurium: a quantitative analysis. J. Bacteriol 180, 4056–4067. [PubMed: 9696751]

(22). Barak Z, Chipman DM, and Gollop N (1987) Physiological implications of the specificity of acetohydroxy acid synthase isozymes of enteric bacteria. J. Bacteriol 169, 3750–3756. [PubMed: 3301814]

(23). Dailey F, and Cronan J (1986) Acetohydroxy acid synthase I, a required enzyme for isoleucine and valine biosynthesis in Escherichia coli K-12 during growth on acetate as the sole carbon source. J. Bacteriol 165, 453–460. [PubMed: 3511034]

(24). Kaplun A, Vyazmensky M, Zherdev Y, Belenky I, Slutzker A, Mendel S, Barak Z, Chipman DM, and Shaanan B (2006) Structure of the Regulatory Subunit of Aceto Hydroxy Acid Synthase isozyme III from Escherichia coli. J. Mol. Biol 357, 951–963. [PubMed: 16458324]

(25). Petkowski JJ, Chruszcz M, Zimmerman MD, Zheng H, Skarina T, Onopriyenko O, Cymborowski MT, Koclega KD, Savchenko A, Edwards A, and Minor W (2007) Crystal structures of TM0549 and NE1324–two orthologs of E. coli AHAS isozyme III small regulatory subunit. Protein Sci 16, 1360–7. [PubMed: 17586771]

(26). Aravind L, and Koonin EV (1999) Gleaning non-trivial structural, functional and evolutionary information about proteins by iterative database searches. J. Mol. Biol 287, 1023–1040. [PubMed: 10222208]

(27). Chipman DM, and Shaanan B (2001) The ACT Domain family. Curr. Opin. Struct. Biol 11, 694–700. [PubMed: 11751050]

(28). Lang EJ, Cross PJ, Mittelstädt G, Jameson GB, and Parker EJ (2014) Allosteric ACTion: the varied ACT domains regulating enzymes of amino-acid metabolism. Curr. Opin. Struct. Biol 29, 102–111. [PubMed: 25543886]

(29). Grant GA (2006) The ACT Domain: A Small Molecule Binding Domain and Its Role as a Common Regulatory Element. J. Biol. Chem 281, 33825–33829. [PubMed: 16987805]

(30). Schuller DJ, Grant GA, and Banaszak LJ (1995) The allosteric ligand site in the Vmax-type cooperative enzyme phosphoglycerate dehydrogenase. Nat. Struct. Biol 2, 69–76. [PubMed: 7719856]

(31). Karanth NM, and Sarma SP (2013) The coil-to-helix transition in IlvN regulates the allosteric control of Escherichia coli acetohydroxyacid synthase I. Biochemistry 52, 70–83. [PubMed: 23205845]

(32). Vyazmensky M, Zherdev Y, Slutzker A, Belenky I, Kryukov O, Barak Z, and Chipman DM (2009) Interactions between large and small subunits of different acetohydroxyacid synthase isozymes of Escherichia coli. Biochemistry 48, 8731–8737. [PubMed: 19653643]

(33). Mitra A, Chakrabarti KS, Shahul Hameed MS, Srinivas KV, Senthil Kumar G, and Sarma SP (2005) High level expression of peptides and proteins using cytochrome b5 as a fusion host. Protein Expression Purif 41, 84–97.

(34). Megha Karanth N, Mitra A, and Sarma SP (2009) Solution NMR studies of Aceto Hydroxy Acid Synthase I: Identification of the sites of inter-subunit interactions using multidimensional NMR methods. J. Mol. Catal. B: Enzym 61, 7–13.

(35). McCoy AJ, Grosse-Kunstleve RW, Adams PD, Winn MD, Storoni LC, and Read RJ (2007) Phaser crystallographic software. J. Appl. Crystallogr 40, 658–674. [PubMed: 19461840]

(36). Winn MD, et al. (2011) Overview of the CCP4 suite and current developments. Acta Crystallogr., Sect. D: Biol. Crystallogr 67, 235–242. [PubMed: 21460441]

(37). Matthews BW (1968) Solvent content of protein crystals. J. Mol. Biol 33, 491–497. [PubMed: 5700707]

(38). Murshudov GN, Vagin AA, and Dodson EJ (1997) Refinement of macromolecular structures by the maximum-likelihood method. Acta Crystallogr., Sect. D: Biol. Crystallogr 53, 240–255. [PubMed: 15299926]

(39). Perrakis A, Harkiolaki M, Wilson KS, and Lamzin VS (2001) ARP/wARP and molecular replacement. Acta Crystallogr., Sect. D: Biol. Crystallogr 57, 1445–1450. [PubMed: 11567158]

(40). Schomaker V, and Trueblood KN (1968) On the rigid-body motion of molecules in crystals. Acta Crystallogr., Sect. B: Struct. Crystallogr. Cryst. Chem 24, 63–76.

(41). Adams PD, et al. (2010) PHENIX: a comprehensive Python- based system for macromolecular structure solution. Acta Crystallogr., Sect. D: Biol. Crystallogr 66, 213–221. [PubMed: 20124702]

(42). PyMOL Molecular Graphics System, version 1.8 (2015) Schrödinger, LLC.

(43). Pettersen EF, Goddard TD, Huang CC, Couch GS, Greenblatt DM, Meng EC, and Ferrin TE (2004) UCSF Chimera – a visualization system for exploratory research and analysis. J. Comput. Chem 25, 1605–1612. [PubMed: 15264254]

(44). Koradi R, Billeter M, and Wüthrich K (1996) MOLMOL: a program for display and analysis of macromolecular structures. J. Mol. Graphics 14, 51–55.

(45). Rother K, Hildebrand PW, Goede A, Gruening B, and Preissner R (2009) Voronoia: analyzing packing in protein structures. Nucleic Acids Res 37, D393–D395. [PubMed: 18948293]

(46). Dundas J, Ouyang Z, Tseng J, Binkowski A, Turpaz Y, and Liang J (2006) CASTp: computed atlas of surface topography of proteins with structural and topographical mapping of functionally annotated residues. Nucleic Acids Res 34, W116–W118. [PubMed: 16844972]

(47). Demeler B, and Gorbet GE (2016) Analytical Ultra- centrifugation, pp 119–143, Springer.

(48). Demeler B, Gorbet G, Zollars D, Dubbs B, Brookes E, and Cao W (2017) UltraScan-III version 4.0: A comprehensive data analysis software package for analytical ultracentrifugation experiments (http://www.ultrascan3.uthscsa.edu).

(49). Demeler B (2010) Methods for the design and analysis of sedimentation velocity and sedimentation equilibrium experiments with proteins. Curr. Protoc. Protein Sci, 7.13.1–7.13.24. [PubMed: 20814934]

(50). Brookes E, Cao W, and Demeler B (2010) A two- dimensional spectrum analysis for sedimentation velocity experiments of mixtures with heterogeneity in molecular weight and shape. Eur. Biophys. J 39, 405–414. [PubMed: 19247646]

(51). Brookes E, and Demeler B (2006) Genetic Algorithm Optimization for Obtaining Accurate Molecular Weight Distributions from Sedimentation Velocity Experiments. Analytical Ultracentrifugation VIII, pp 33–40.

(52). Brookes EH, and Demeler B (2007) Parsimonious regularization using genetic algorithms applied to the analysis of analytical ultracentrifugation experiments. Proceedings of the 9th annual conference on genetic and evolutionary computation, pp 361–368.

(53). Demeler B, and van Holde KE (2004) Sedimentation velocity analysis of highly heterogeneous systems. Anal. Biochem 335, 279–288. [PubMed: 15556567]

(54). Biasini M, Bienert S, Waterhouse A, Arnold K, Studer G,Schmidt T, Kiefer F, Cassarino TG, Bertoni M, Bordoli L, and Schwede T (2014) SWISS-MODEL: modelling protein tertiary and quaternary structure using evolutionary information. Nucleic Acids Res 42, W252–W258. [PubMed: 24782522]

(55). Benkert P, Tosatto SCE, and Schomburg D (2008) QMEAN: A comprehensive scoring function for model quality assessment. Proteins: Struct., Funct., Genet 71, 261–277. [PubMed: 17932912]

(56). Ramachandran GN, Ramakrishnan C, and Sasisekharan V (1963) Stereochemistry of polypeptide chain configurations. J. Mol. Biol 7, 95–99. [PubMed: 13990617]

(57). Bennett MJ, Schlunegger MP, and Eisenberg D (1995) 3D domain swapping: A mechanism for oligomer assembly. Protein Sci 4, 2455–2468. [PubMed: 8580836]

(58). Schreiter ER, Sintchak MD, Guo Y, Chivers PT, Sauer RT, and Drennan CL (2003) Crystal structure of the nickel- responsive transcription factor NikR. Nat. Struct. Mol. Biol 10, 794–799.

(59). Zhang S, Huang T, Ilangovan U, Hinck AP, and Fitzpatrick PF (2014) The Solution Structure of the Regulatory Domain of Tyrosine Hydroxylase. J. Mol. Biol 426, 1483–1497. [PubMed: 24361276]

(60). Dey S, Hu Z, Xu XL, Sacchettini JC, and Grant GA (2007) The Effect of Hinge Mutations on Effector Binding and Domain Rotation in Escherichia coli D-3-Phosphoglycerate Dehydrogenase. J. Biol. Chem 282, 18418–18426. [PubMed: 17459882]

(61). Gao M, and Skolnick J (2012) The distribution of ligand- binding pockets around protein-protein interfaces suggests a general mechanism for pocket formation. Proc. Natl. Acad. Sci. U. S. A 109, 3784–3789. [PubMed: 22355140]

(62). Wallace AC, Laskowski RA, and Thornton JM (1995) LIGPLOT: a program to generate schematic diagrams of protein-ligand interactions. Protein Eng., Des. Sel 8, 127–134.

(63). Mendel S, Elkayam T, Sella C, Vinogradov V, Vyazmensky M, Chipman DM, and Barak Z (2001) Aceto Hydroxy Acid Synthase: a proposed structure for regulatory subunits supported by evidence from mutagenesis. J. Mol. Biol 307, 465–477. [PubMed: 11243831]

(64). Mitra A, and Sarma SP (2008) Escherichia coli ilvN interacts with the FAD binding domain of ilvB and activates the AHAS I enzyme. Biochemistry 47, 1518–1531. [PubMed: 18193896]

(65). Xie Y, Wen X, Zhao D, Niu C, Zhao Y, Qi H, and Xi Z (2018) Interactions between the ACT Domains and Catalytic Subunits of Acetohydroxyacid Synthases (AHASs) from Different Species. ChemBioChem 19, 2387–2394. [PubMed: 30225979]

(66). Vinogradov V, Vyazmensky M, Engel S, Belenky I, Kaplun A, Kryukov O, Barak Z, and Chipman DM (2006) Aceto Hydroxy Acid Synthase isozyme I from Escherichia coli has unique catalytic and regulatory properties. Biochim. Biophys. Acta, Gen. Subj 1760, 356–363.

(67). Yoshida A, Tomita T, Kuzuyama T, and Nishiyama M (2010) Mechanism of Concerted Inhibition of α2β2-type Hetero- oligomeric Aspartate Kinase from Corynebacterium glutamicum. J. Biol. Chem 285, 27477–27486. [PubMed: 20573952]

(68). Robin AY, Cobessi D, Curien G, Robert-Genthon M, Ferrer J-L, and Dumas R (2010) A new mode of dimerization of allosteric enzymes with ACT domains revealed by the crystal structure of the aspartate kinase from Cyanobacteria. J. Mol. Biol 399, 283–293. [PubMed: 20398676]

(69). Fan Y, Cross PJ, Jameson GB, and Parker EJ (2018) Exploring modular allostery via interchangeable regulatory domains. Proc. Natl. Acad. Sci. U. S. A 115, 3006–3011. [PubMed: 29507215]

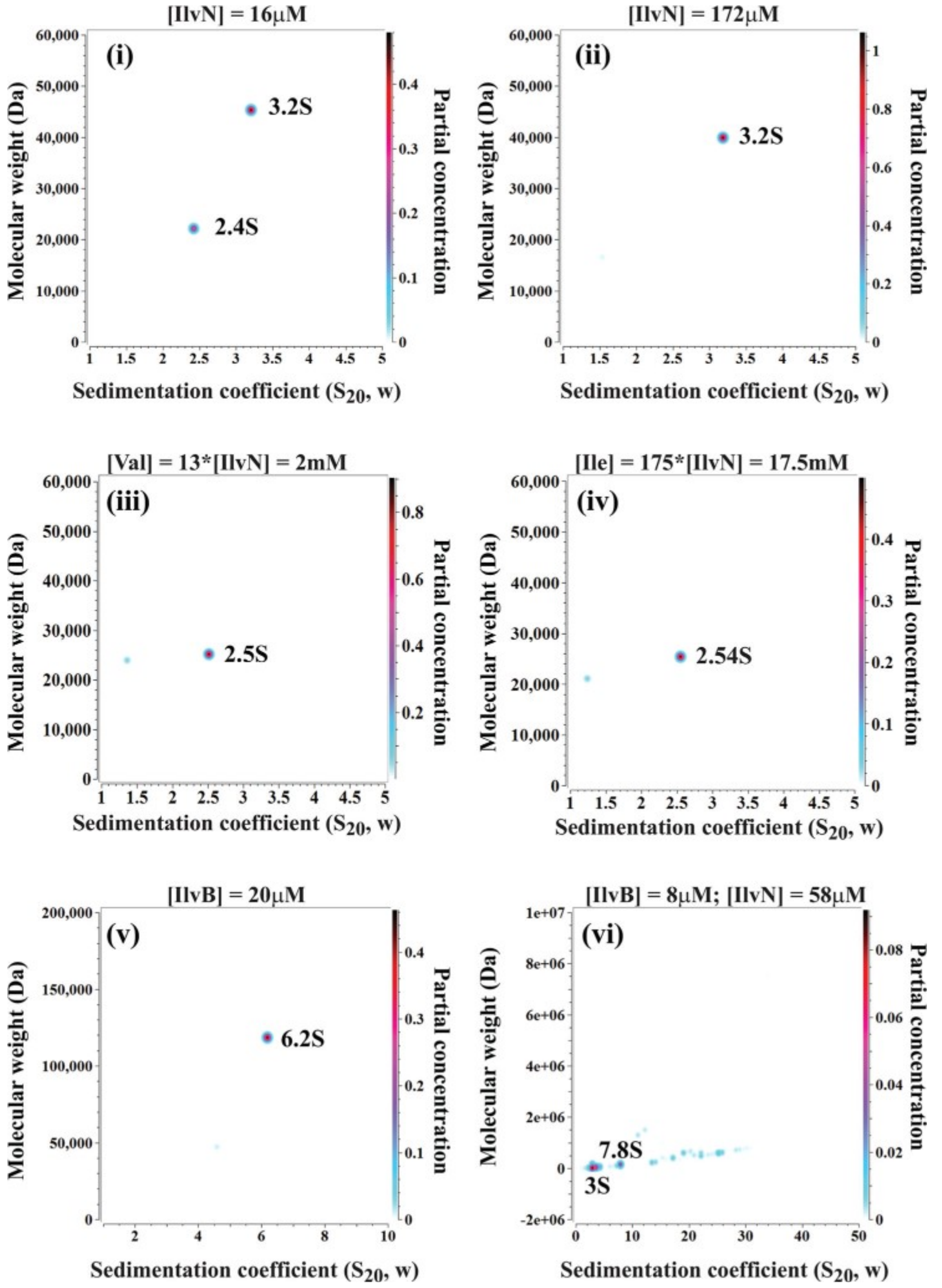

Figure 1.

Pseudo-three-dimensional plots for GA analysis of SV-AUC data. (i and ii) GA distribution plots at different concentrations of IlvN. IlvN shows a dimer-tetramer equilibrium at low concentrations (≤16 μM). At higher concentration (~172 μM), only a tetrameric species sedimenting at 3.2 S is observed. (iii and iv) GA analysis indicates IlvN is a dimer in solution, when bound to valine and isoleucine (at high concentrations). (v and vi) Results of GA analysis of SV-AUC data for IlvB and the AHAS I holoenzyme. IlvB sediments as a dimer, and the holoenzyme as a heterohexamer (2CSU:4RSU). The species at 3 S is free ilvN sedimenting as a tetrameric species. See the text for details.

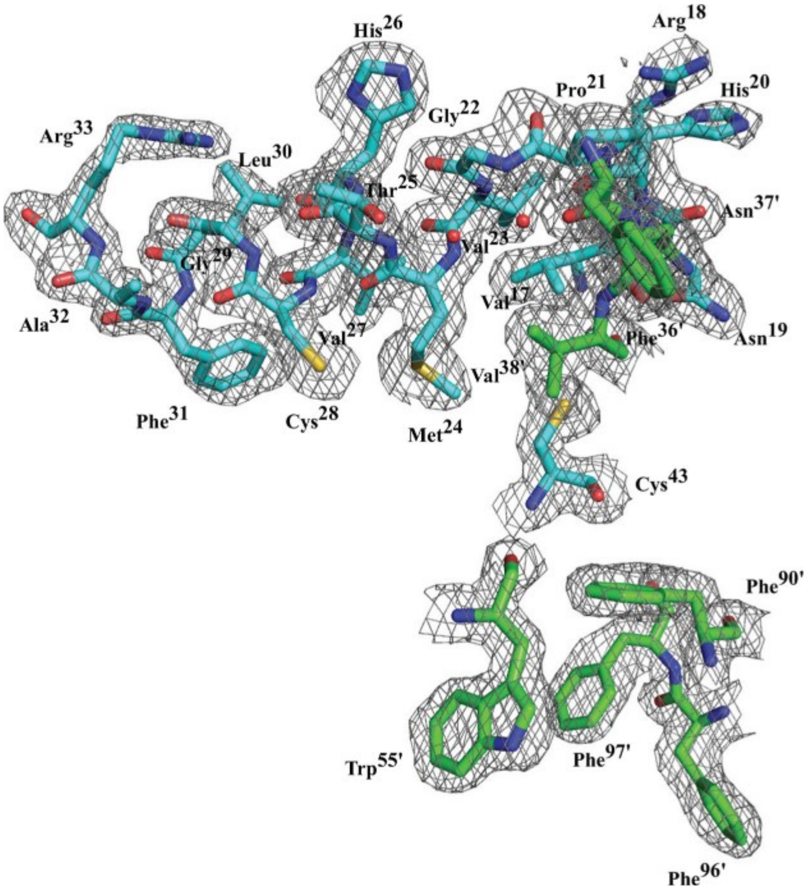

Figure 2.

SIGMAA-weighted $2F_o - F_c$ electron density map of crystal 1a contoured at a level of 1σ. Residues of chain A are colored cyan, and those of chain B green. The positions of aromatic rings and side chains of polar, charged, and aliphatic residues are well-defined in the electron density map.

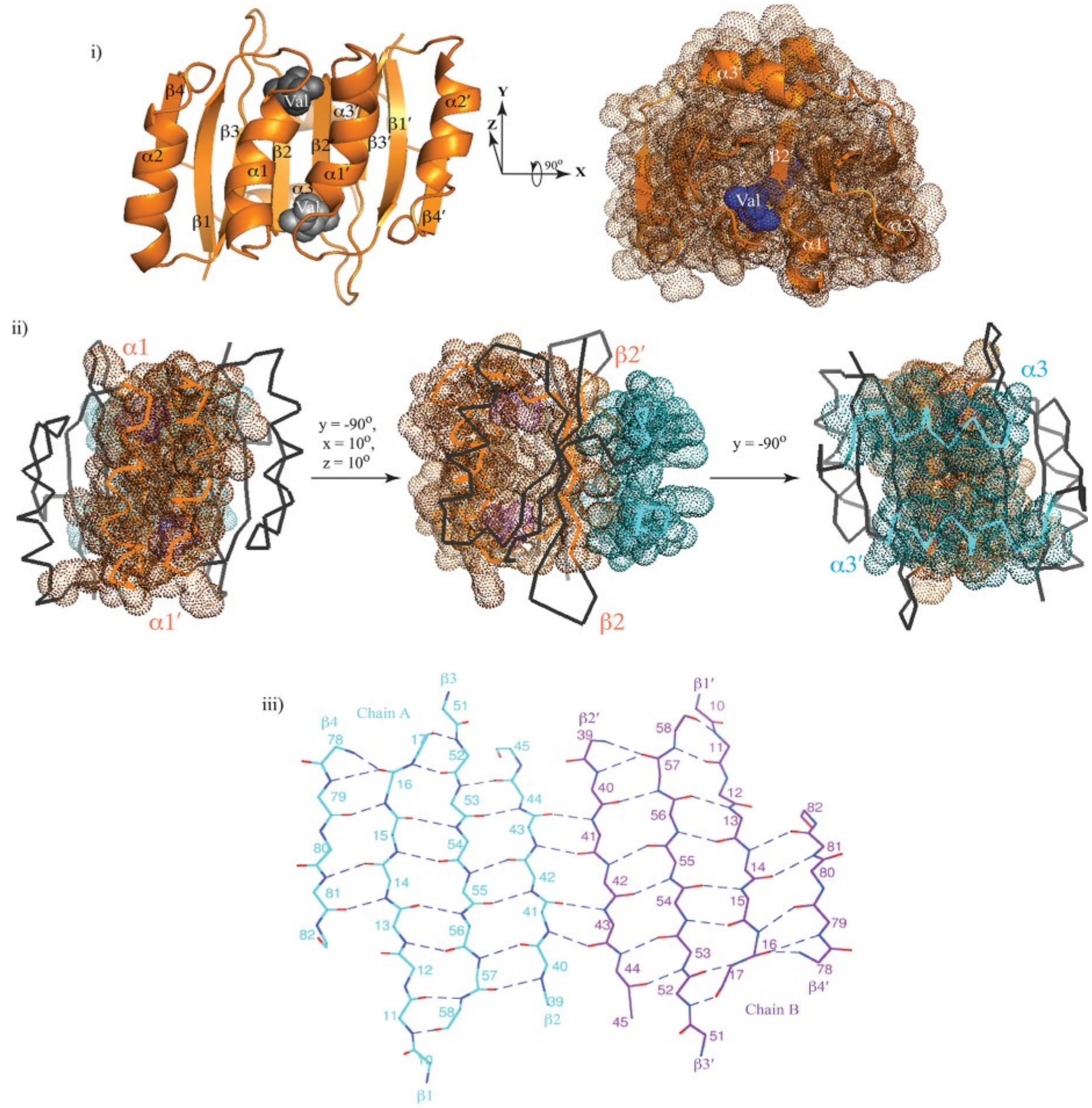

Figure 3.

Quaternary structure and molecular packing. (i) IlvN dimer in cartoon representation (left). Valine molecules located in the binding pockets at the dimer interface are colored dark gray. The secondary structural elements for chains A and B (denoted with primes) are as indicated. Dot representation of the IlvN dimer surface after a 90° rotation around the *x*-axis (right). A tight molecular packing can be observed in the interior of the molecule. The valine ligand is colored blue for the sake of clarity. (ii) Three views of IlvN showing the tight packing at the dimer interface. The backbone is shown in ribbon representation. Backbone and side-chain atoms of residues at the interface are shown in dot representation. Secondary structural elements $\alpha 1$ and $\beta 2$ are colored orange, and $\alpha 3$ is colored blue. Valine molecules are colored magenta. Other regions of the molecule are colored black. The tight packing at the interface results in a buried surface area of 2676 Å^2. See the text for details. (iii)

Hydrogen bonding pattern that stabilizes the eight-stranded *β* sheet at the core of the ACT fold of IlvN. Chain A is colored cyan, while chain B is colored purple. Residues of both chains are numbered in sequence, and hydrogen bonds are shown as dashed lines.

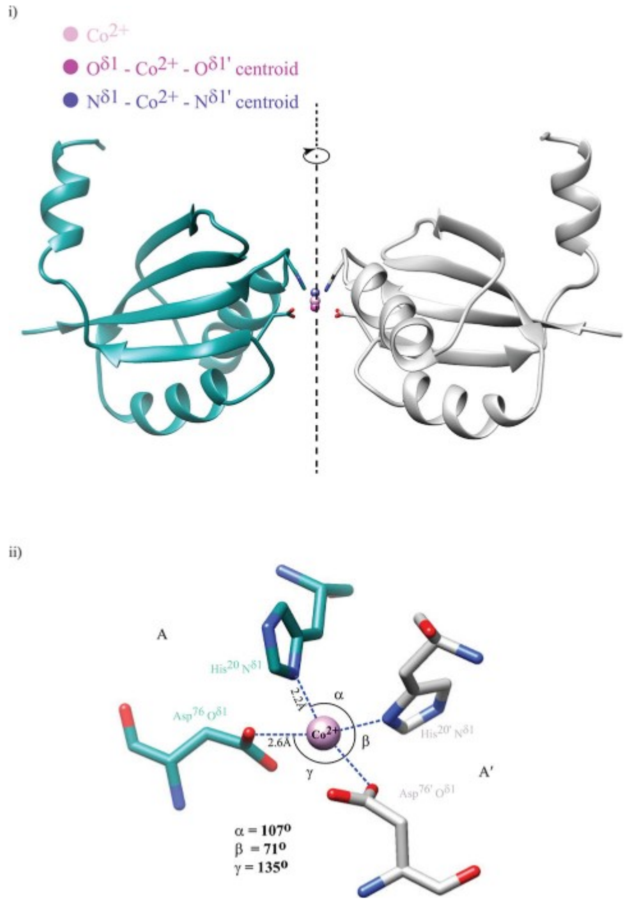

Figure 4.

Co^{2+} binding by IlvN in crystal 2. (i) One Co^{2+} ion was found to be associated with each dimer. The Co^{2+} ion is located on the crystallographic 2-fold axis. The centroids of the liganding atoms are co-linear with the Co^{2+} ion on the axis. (ii) Co^{2+} is coordinated in a distorted tetrahedral arrangement as defined by the bond angles and bond lengths. The residues of chain A are colored cyan, while those of the corresponding symmetry mate are colored light gray.

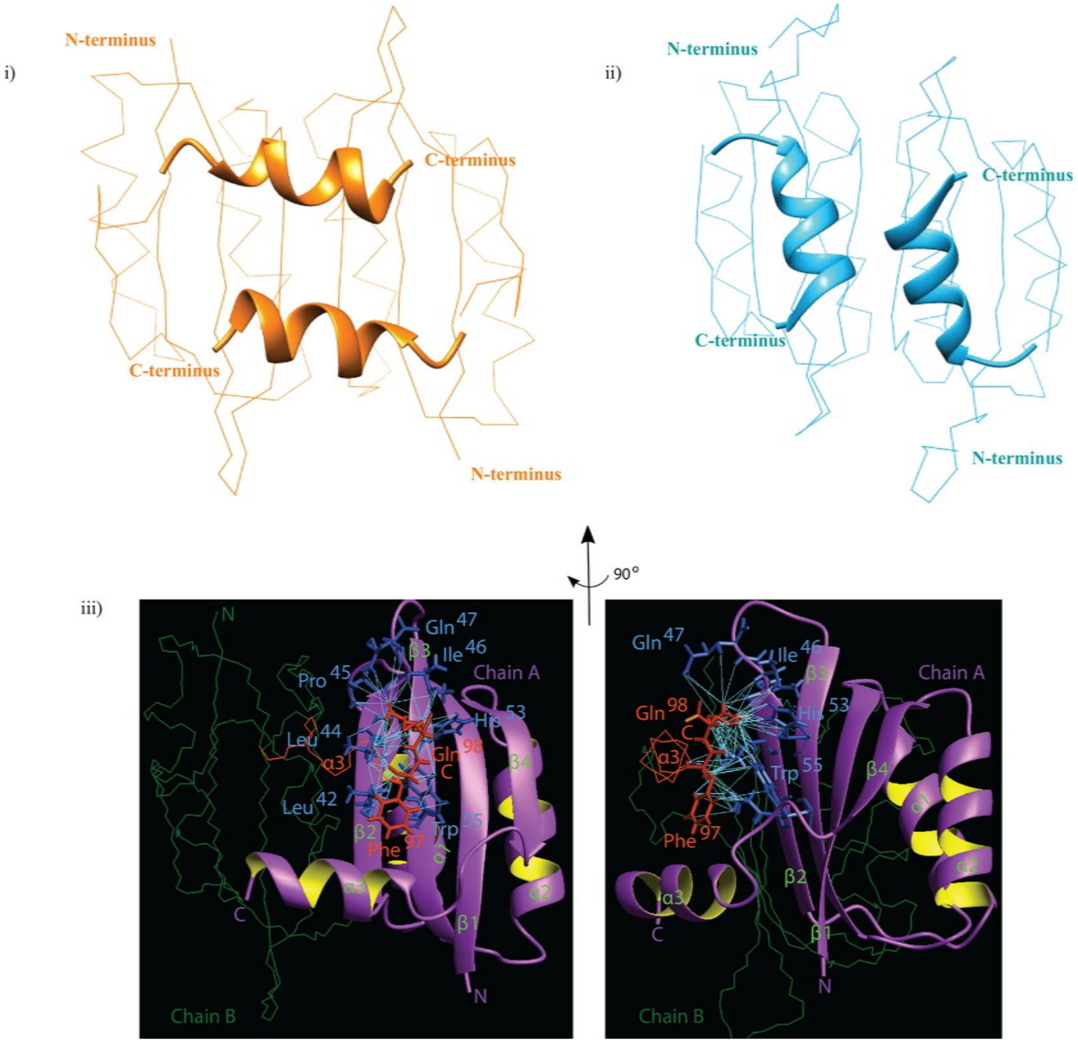

Figure 5.

Backbone presentation of X-ray (i) and solution NMR-derived structures of IlvN (PDB entry 2LVW) (ii). The two differ in the orientation of C-terminal helix $\alpha 3$. With this exception, excellent agreement is seen in overall topology and secondary structure definition between the structures in solution and in the crystal. (iii) Crystallographic structure of IlvN highlighting the defining long-range NOE correlations between residues from the C-terminus of helix $\alpha 3$ of chain B (residues Phe^{97} and Gln^{98}) and residues in the β sheet of chain A (Leu^{42}, Leu^{44}, Pro^{45}, Ile^{46}, Gln^{47}, His^{53}, and Trp^{55}). The backbone and side chain of residues of helix $\alpha 3$ of chain B are colored orange, and the rest of chain B is colored green. Chain A is shown in cartoon representation, and the backbone and side chain of the residues listed above are colored blue. The expected NOEs between pairs of interprotomer dipolar coupled protons are connected by cyan-colored lines. The upper distance limit for expected NOE correlations was set to 5 Å. Back-calculation of interproton distances was carried out using MOLMOL. These predicted correlations are not observed in any of the NOESY data sets we examined.

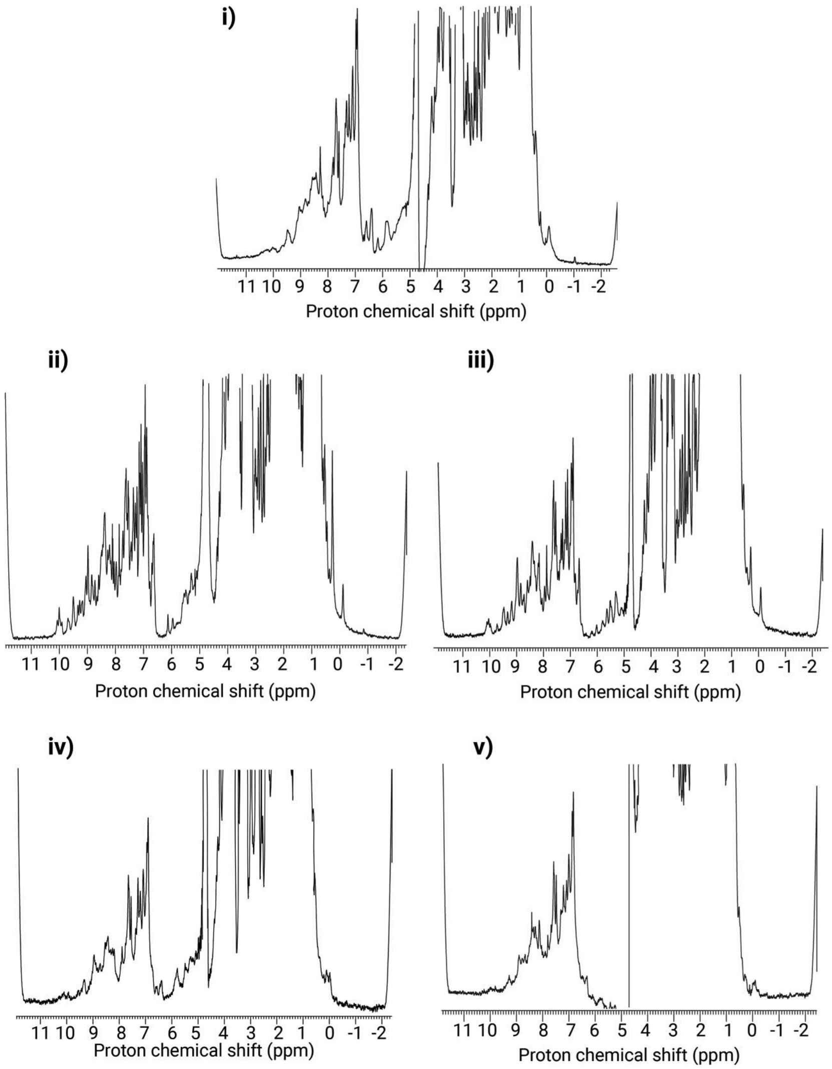

Figure 6.

One-dimensional spectra of IlvN in (i) the free form and in the presence of (ii) 5 mM Val, (iii) 10 mM Ile, (iv) 20 mM Leu, and (v) 20 mM Thr. The change in line shapes is indicative of ligand binding in the case of Val and Ile. No change is observed in the case of the two remaining *β*-branched amino acids.

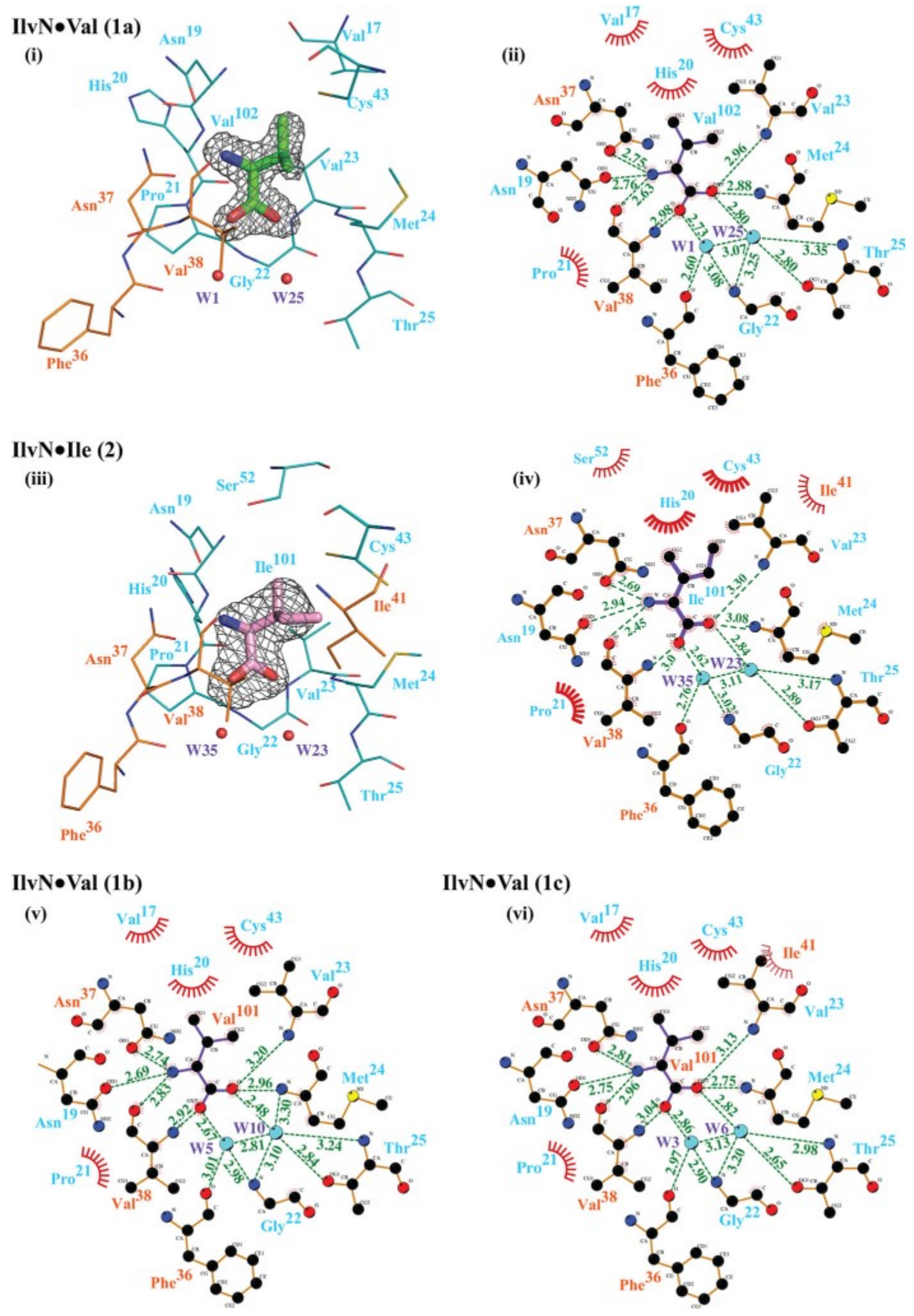

Figure 7.

Ligand binding pockets of IlvN in the four crystal forms. $F_\mathrm{o} - F_\mathrm{c}$ omit maps defining the electron densities (contoured at the 5σ level in PyMOL) for the ligands valine in crystal form 1a and isoleucine in crystal form 2 are shown in panels i and iii, respectively. The binding pocket residues of chain B are colored blue, and those of chain A orange. The corresponding two-dimensional projections (ligplots) in which residues in chains B and A stabilize the ligand in the binding pocket are identified in panels ii and iv−vi. Direct and water-mediated hydrogen bonds between the protein and ligand are shown with dashed lines (colored green). The corresponding hydrogen bond lengths between interacting atoms are indicated in the figure. Hydrophobic interactions between protein and ligand are indicated by eyelashes. Water molecules are labeled W. The bottom panel shows the corresponding ligplots for crystal forms 1b and 1c.

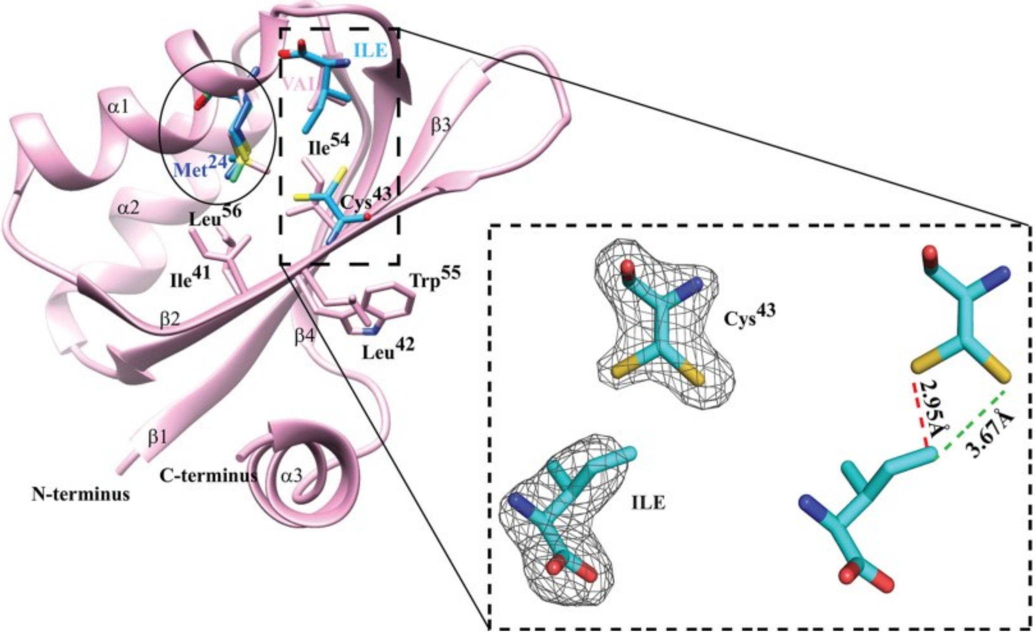

Figure 8.

Section of the IlvN dimer showing the conformations of the CH $^{\varepsilon}{}_3$ of the Met^{24} side chain (circled) in the four crystal structures. Met^{24} from each structure is colored differently. The ligands valine and isoleucine are colored light pink and blue, respectively. The residues in the vicinity, e.g., Leu^{56}, Ile^{41}, Ile^{54}, Trp^{55}, and Leu^{42}, are labeled. Different orientations of Met^{24} depict the plasticity of the binding pocket, which in turn is permitted by the absence of steric clashes with neighboring residues. The inset shows the side-chain conformations of Cys^{43} in the IlvN·Ile complex. $F_o - F_c$ omit maps of the electron densities (contoured at the 5σ level in PyMOL) that define the conformations of the ligand isoleucine and Cys^{43} are shown on the left. Two distinguishable orientations of Cys^{43} can be observed. The distance between Ile$^{C\delta}$1 and S^{γ} of Cys^{43} is 2.95 Å (red). To avoid a steric clash, the χ_1 dihedral angle of Cys^{43} changes form *gauche*$^-$ (−61.4°) to trans (179.5°). This places the C$^{\delta}$1 atom 3.67 Å from the sulfur atom.

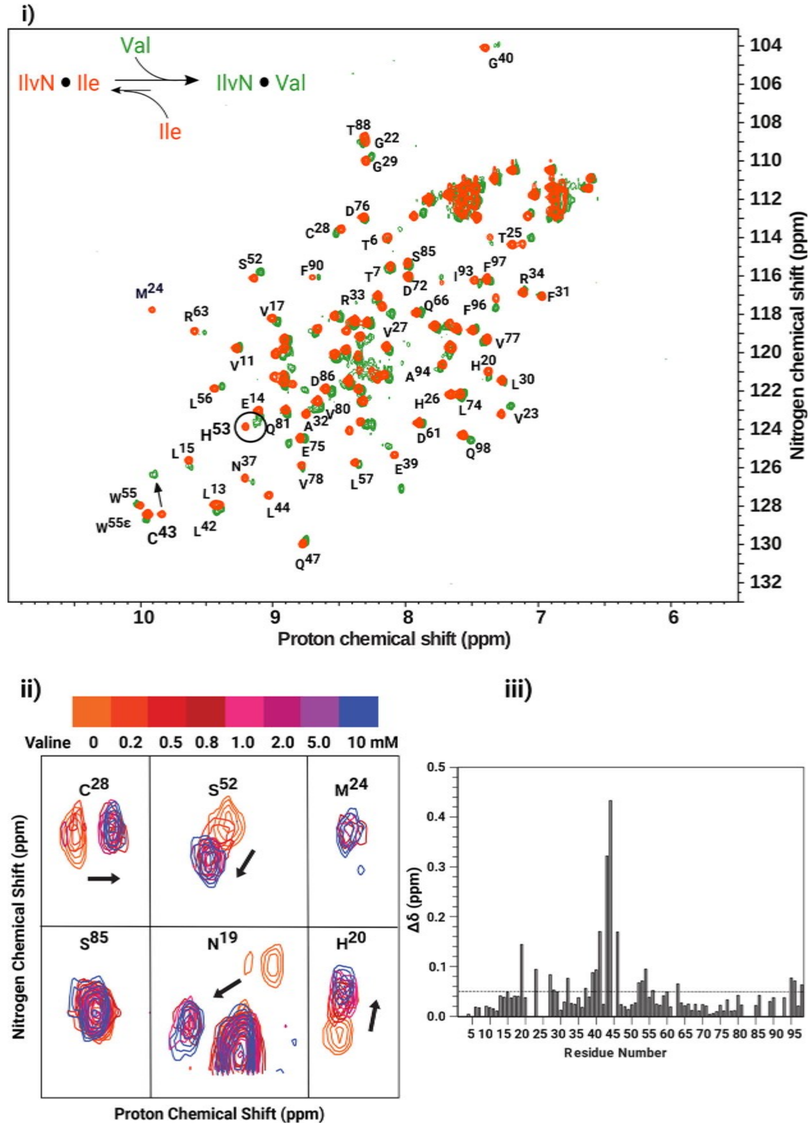

Figure 9.

(i) Overlay of ^{1}H–^{15}N HSQC spectra of IlvN·Ile and IlvN·Val complexes. Spectra were acquired on samples of the IlvN·Ile complex (10 mM Ile, orange spectrum) to which 5 mM Val was added (green spectrum). The change in the chemical shift of Cys^{43} in going from an isoleucine complex to a valine complex is indicated by an arrow. The correlation peaks for His^{53} are encircled. (ii) Overlay of select regions of ^{1}H–^{15}N correlation spectra showing the changes in chemical shift positions of residues in the binding pocket (Asn^{19}, His^{20}, and Ser^{52}) and helix $\alpha 1$ (Met^{24} and Cys^{28}). Ser^{85}, which is far from the binding site, is unperturbed upon ligand exchange and served as an internal calibrant. (iii) Plot of the chemical shift differences ($\Delta\delta$ in parts per million) between IlvN·Val and IlvN·Ile complexes as a function of residue number. Residues in the binding pocket and those that exhibit conformational heterogeneity show chemical shift changes of >0.05 ppm.

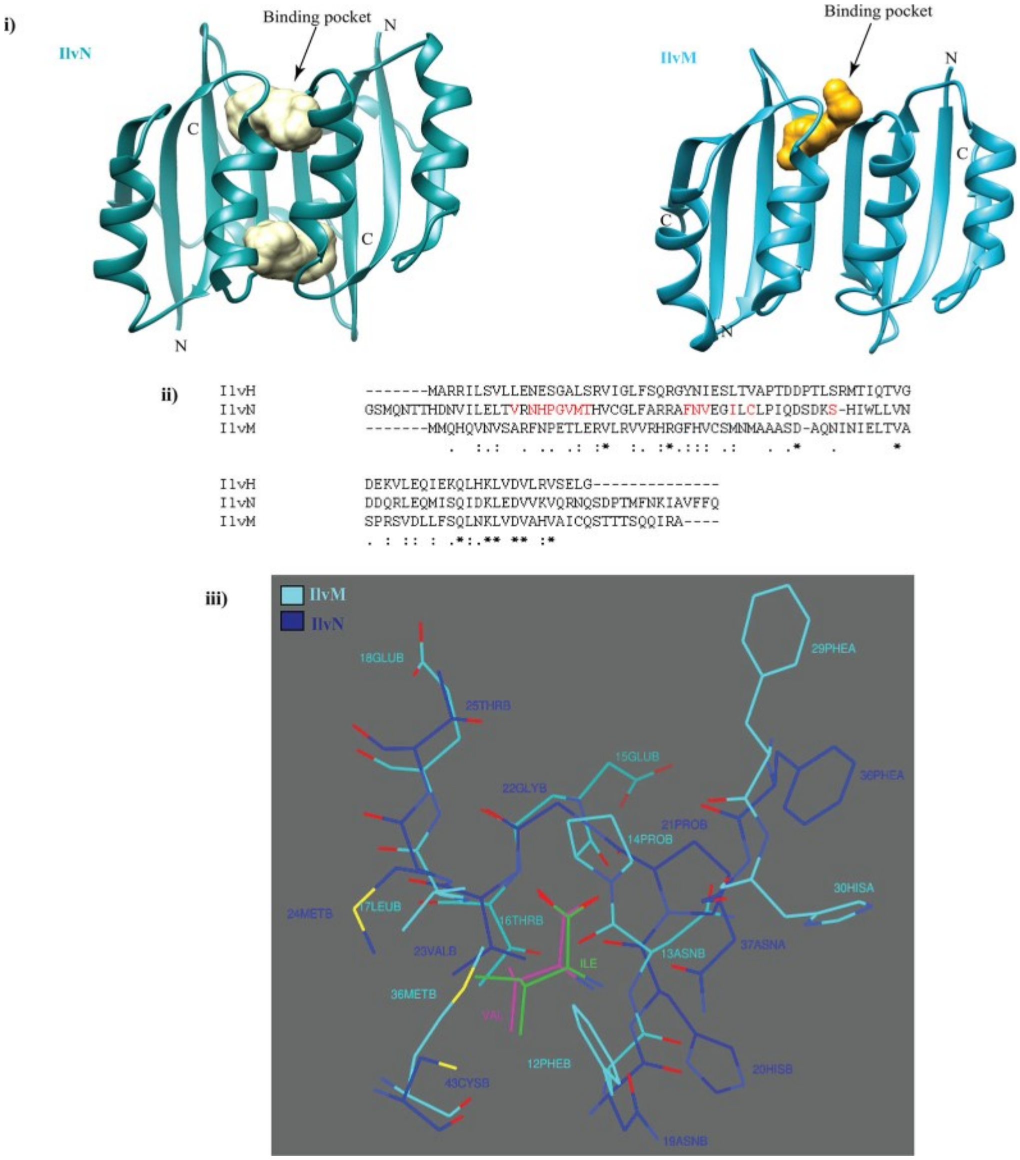

```
IlvH        -------MARRILSVLLENESGALSRVIGLFSQRGYNIESLTVAPTDDPTLSRMTIQTVG
IlvN        GSMQNTTHDNVILELTVRNHPGVMTHVCGLFARRAFNVEGILCLPIQDSDKS-HIWLLVN
IlvM        -------MMQHQVNVSARFNPETLERVLRVVRHRGFHVCSMNMAAASD-AQNINIELTVA
                     .  :.:  . .. .: :*  :. :*.::: .:   . .*   .      *

IlvH        DEKVLEQIEKQLHKLVDVLRVSELG-------------
IlvN        DDQRLEQMISQIDKLEDVVKVQRNQSDPTMFNKIAVFFQ
IlvM        SPRSVDLLFSQLNKLVDVAHVAICQSTTTSQQIRA----
            . : :: : .*:.** ** :*
```

Figure 10.

(i) Comparison of the ligand binding pocket (cavity) volumes of IlvN (crystal 1a) and a model of IlvM derived from the structure of the N-terminal domain of IlvH (PDB entry 2f1f). The cavities are shown as hollow spheres that are colored white (IlvN) and ochre (IlvM). The best fit sequence alignment among IlvM, IlvN, and the N-terminal domain of IlvH is shown in panel ii. Residues in IlvN that line the binding pocket are colored red. (iii) Overlay of the binding pocket of IlvN with the corresponding region of IlvM. IlvN residues are colored navy blue, while those of IlvM cyan. The ligands valine and isoleucine are colored magenta and green, respectively. The presence of Phe^{12} and Met^{36} in the IlvM sequence in place of Asn^{19} and Cys^{43}, respectively, leads to steric crowding in the Ile/Val binding pocket of IlvM. Residues are numbered in sequence with chain IDs as suffixes.

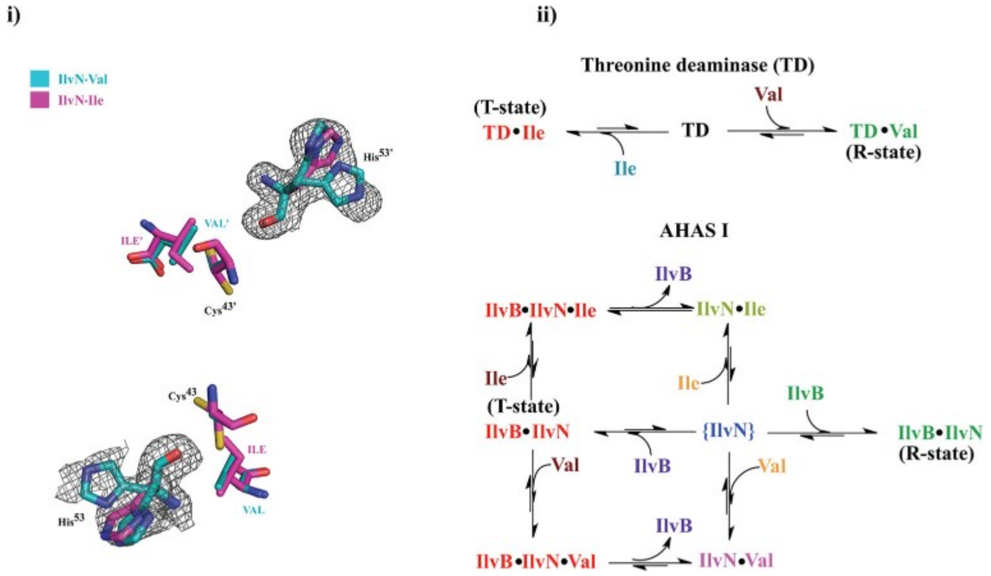

Figure 11.

(i) $F_{\mathrm{o}} - F_{\mathrm{c}}$ omit maps showing the electron densities that define the side-chain conformations of His^{53} in the IlvN·Val complex (contoured at the 2σ level in PyMOL). Concerted changes in the conformations of Cys^{43} and His^{53} in both protomers of the molecule are observed. Residues in the IlvN·Val complex are colored cyan, and those in the IlvN·Ile complex are colored magenta. The two chains can be distinguished by residue labels with and without primes. (ii) Schematic representation of the activation and inhibition mechanisms of threonine deaminase (top) and that proposed for AHAS I (bottom) by the end products of the branched-chain amino acid biosynthesis pathway. The schemes indicate the roles of valine and isoleucine in the associative and dissociative mechanisms.

Table 1.

Data Collection and Refinement Statistics[a]

	IlvN·Val			IlvN·Ile
crystal form	**1a** (5YPP)	**1b** (5YPW)	**1c** (5YPY)	**2** (5YUM)
Data Collection				
beamline	ESRF BM-14			home source
space group	$P2_1$	$P2_1$	C2	$H32$
wavelength (Å)	0.9537	0.9537	0.9537	1.5418
range (Å)	57.2–1.9 (1.94–1.9)	62.20–2.30 (2.38–2.30)	62.72–1.97 (2.01–1.97)	57.88–2.43 (2.52–2.43)
a (Å)	66.03	63.04	110.52	89.62
b (Å)	80.62	74.67	74.51	89.62
c (Å)	66.04	88.81	63.27	86.87
β (deg)	119.99	99.37	97.58	90.0
total no. of reflections	180214 (11684)	132750 (13025)	143900 (8590)	54736 (5533)
no. of reflections in working/test set	44797/2052	34528/1769	34282/1836	4834/353
no. of unique reflections	47251 (3094)	36346 (3568)	36151 (2421)	5202 (534)
completeness (%)	99.8 (100)	100 (100)	99.7 (95.7)	100 (100)
$\langle I/\sigma \rangle$	15.1 (2.5)	5.9 (2.0)	5.2 (1.1)	20.7 (4.3)
R_{pim}[b]	0.039 (0.402)	0.114 (0.6)	0.096 (0.589)	0.031 (0.195)
R_{meas}[c]	0.057 (0.601)	0.166 (0.876)	0.145 (0.893)	0.075 (0.037)
$CC_{1/2}$	0.999 (0.672)	0.991 (0.775)	0.993 (0.764)	0.999 (0.949)
anomalous completeness (%)	-	-	-	100 (71)
anomalous multiplicity	-	-	-	5.3 (5.5)
DelAnom $CC_{1/2}$	-	-	-	0.236 (−0.008)
Refinement				
no. of non-hydrogen atoms	4671	5818	3020	766
no. of water molecules	134	83	68	26
R_{work} (%)[d]	14.84	18.29	19.79	19.10
R_{free} (%)[d]	17.03	23.34	24.19	22.61

		IlvN·Val		**IlvN·Ile**
mean B-factor for all atoms (Å^2)	42.3	47.0	52.0	53.0
B-factor estimated from a Wilson plot (Å^2)	30.9	30.0	28.0	40.9
RMSD from ideality				
bond lengths (Å)	0.003	0.008	0.0177	0.003
bond angles (deg)	0.565	1.100	1.430	0.621
Ramachandran analysis[56]				
most favored regions (%)	97.64	99.43	98.58	97.73
additionally favored regions (%)	1.96	0.57	0.85	2.27
outliers (%)	0.39	0	0.57	0

[a] Values in parentheses refer to those for the highest-resolution shell.

[b] $$R_{\text{pim}} = \sqrt{(1/n-1)}\frac{\sum_{hkl}\sum_{i=1}^{n}\left|I_i(hkl) - \bar{I}(hkl)\right|}{\sum_{hkl}\sum_{i=1}^{n} I_i(hkl)}.$$

[c] $$R_{\text{meas}} = \sqrt{(n/n-1)}\frac{\sum_{hkl}\sum_{i=1}^{n}\left|I_i(hkl) - \bar{I}(hkl)\right|}{\sum_{hkl}\sum_{i=1}^{n} I_i(hkl)}.$$

[d] $$R_{\text{work/free}} = \frac{\sum_{hkl}\left\|F_O(hkl)\right| - \left|F_C(hkl)\right\|}{\sum_{hkl}\left|F_O(hkl)\right|}.$$